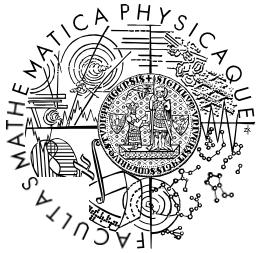

FACULTY
OF MATHEMATICS
AND PHYSICS
Charles University

DOCTORAL THESIS

Udit Acharya

Charge carrier transport in conjugated polymers with controlled morphology

Institute of Macromolecular Chemistry, CAS

Supervisor of the doctoral thesis: RNDr. Jiří Pfleger, CSc.
Study programme: Biophysics, chemical and macromolecular physics

Prague 2023

I declare that I carried out this doctoral thesis independently, and only with the cited sources, literature and other professional sources. It has not been used to obtain another or the same degree.

I understand that my work relates to the rights and obligations under the Act No. 121/2000 Sb., the Copyright Act, as amended, in particular the fact that the Charles University has the right to conclude a license agreement on the use of this work as a school work pursuant to Section 60 subsection 1 of the Copyright Act.

In ..... date ....

Author's signature

To my parents...

Dedication

I would like to express my deepest gratitude and appreciation to all those who have supported and contributed to the completion of my PhD studies and this thesis. This research endeavor has been an incredible journey, and I am truly grateful for the assistance and encouragement I have received along the way.

First and foremost, I would like to extend my heartfelt thanks to my supervisor, Dr. Jiri Pfleger, for his invaluable guidance, expertise, and unwavering support throughout the entire PhD studies. His insightful feedback, patience, and dedication have been instrumental in shaping this work and pushing me to strive for excellence.

I would like to express my sincere appreciation to Dr. Patrycja Bober and her group for providing me with the necessary guidance to pursue my studies.

I am immensely grateful to the Institute of Macromolecular Chemistry, CAS. The academic environment and resources offered by the institution have been essential in conducting this research.

Furthermore, I would like to extend my appreciation to my friends and colleagues who have offered their support, encouragement, and understanding throughout this journey. Your friendship, discussions, and motivation have provided me with the necessary strength to overcome challenges and persevere.

I would like to express my deepest gratitude to my parents and all family members. Their unconditional love, unwavering belief in my abilities, and constant encouragement have been the driving force behind my academic pursuits. Their sacrifices and understanding during this time have been immeasurable.

Special thanks to “The Hatkelaa”. You guys are really awesome.

And last but not the least, my love, Neetu, without whom, it would have not been possible.

To all those who have played a role, big or small, in shaping my research activities and this thesis, I offer my sincere thanks. Your contributions have been invaluable, and I am truly grateful for your support.

Title: Charge carrier transport in conjugated polymers with controlled morphology

Author: Udit Acharya

Department: Institute of Macromolecular Chemistry, CAS

Supervisor: RNDr. Jiří Pfleger, CSc., Institute of Macromolecular Chemistry, CAS

Abstract:

The growing demand for new materials for electronics that could offer novel functionalities for everyday use and for special applications in healthcare and industry, together with concerns about energy consumption, have stimulated an increasing research on electrical properties of conjugated macromolecules. The superiority of these macromolecules arises from their inherent properties based on alternating single and double bonds. In this thesis, charge transport in conducting polymers, namely polypyrrole, poly(*p*-phenylenediamine) and polyaniline, and their composites was investigated with respect to various morphology controlled by oxidant-to-monomer ratio, composite composition and other modifications of their synthesis. Based on a combination of various experimental techniques, like impedance spectroscopy, electron microscopy, electrochemical and optical measurements, the relation between the morphology and charge carrier transport was elucidated. The variable range hopping was found to be a dominant mechanism in the studied polymers. Additionally, metallo-supramolecular polymers have been prepared that offer well-organized structures by complexation of conjugated segments with metal ions. The spectro-electrochemical studies revealed electrochromic phenomena in these polymers. By optimization of the oligomer conjugated sequence, electrochromic properties were tuned and a prototype solid-state electrochromic device was fabricated, showing an efficient and fast electrochromic switching.

Keywords: conducting polymers, charge transport, polarons, variable range hopping, electrochromism

Contents

1. Introduction

Conjugated polymers represent a fascinating class of organic materials which combine electronic and optical properties of semiconductors with mechanical flexibility, easy processing and low cost/low energy consuming manufacturing [1]. They contain alternating sequences of single and double bonds in the polymer backbone, which allow the delocalization of π-electrons along the chain [2]. The morphology of these polymers strongly affects the charge transfer properties and it can be optimized to adapt the polymer performance to various applications [3]. This thesis begins with the in-depth look at conducting polymers, continues with the introduction to various charge transport models applicable to different polymer structures, and ends with an example of well-organized structures of metallo-supramolecular polymers with focus on their electrochromism as the main application.

1.1 Conducting polymers

Conducting polymers refer mostly to π–conjugated polymers capable to transport free charges, which can be generated in the polymer thermally, by photoexcitation or injection [3]. They commonly behave as semiconductors but some of them can reach high electrical conductivity upon doping with various acceptors and donors, even approaching metallic behaviour [2]. The extensive research in conducting polymer field has been continuously growing during the past decades, surging with the Nobel Prize in Chemistry awarded in 2000 to Alan J. Heeger, Alan G. MacDiarmid and Hideki Shirakawa "for the discovery and development of conductive polymers" [3]. Polyaniline (PANI) [4], polyacetylene (PA) [2], polypyrrole (PPy) [5], poly(3,4-ethylenedioxythiophene) (PEDOT) [6] or poly(*p*-phenylenediamine) (PPDA) [7] shown in Fig. 1 are the most well-known examples of conducting polymers capable of achieving a high electrical conductivity and a reasonable chemical stability.

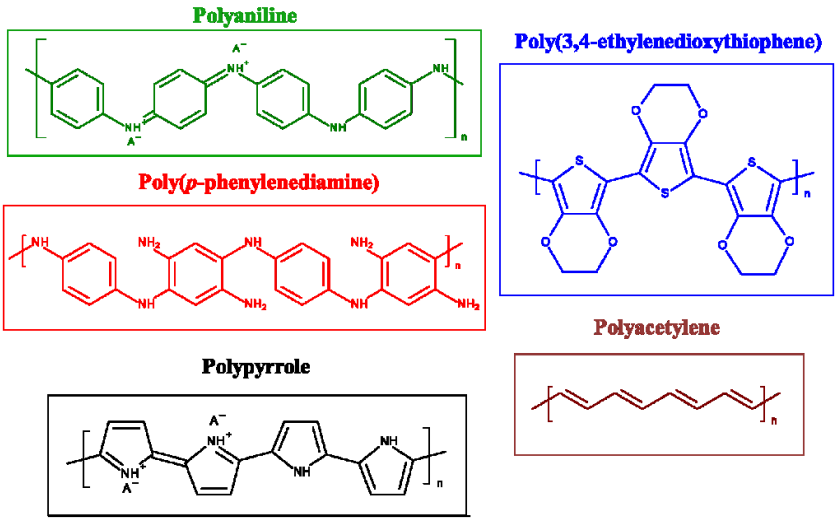

Figure 1. Examples of conducting polymer structures.

The synthesis of these highly conducting polymers can be done typically by an oxidative polymerization, using either chemical or electrochemical roots. The chemical oxidative polymerization uses a corresponding monomer (pyrrole, aniline, etc.) in combination with an oxidizing agent (iron(III) chloride, ammonium peroxodisulfate, etc.) in an aqueous or acidic medium. The product is mostly obtained in the form of powder [7], which is insoluble and not meltable and, hence, difficult to use in practical applications. However, a thin conducting polymer film usually grows on any surface immersed in the polymerization mixture, which makes the fabrication of devices possible. It is one of the most common procedures for obtaining conducting composites [8,9]. Additionally, when water soluble polymers, like polyvinylpyrrolidone, are introduced to the polymerization mixture, colloidal dispersion of conducting polymers are formed, [10,11], which can be later processed by various printing and coating techniques to form conducting films on substrates in an industrial scale. All these three forms of conducting polymers (powders, films, and colloids) have been used in the research reported in this thesis. Electrochemical preparation includes potentiodynamic (cyclic voltammetry), potentiostatic (constant potential) and galvanostatic (constant current) methods and results in polymer films grown on the electrode surface [12].

The chemical structure of conducting polymers comprises of alternating single (σ) and double bonds (π), and polymer chains can be easily oxidized or reduced. They possess a rather small band gap compared to polymers with a saturated backbone (e.g. around 3 eV for PPy) [13] and high mobility of charge carriers. It allows for significant conductivity in the doped state, which can be achieved by electron removal (through oxidation) or introduction (through reduction) to their molecules. Oxidation or reduction can proceed either electrochemically or by doping with various electron acceptors or donors, admixed to the polymer during the preparation or by the diffusion from a solution or vapor phase. The doping process involves redox reaction of polymer molecule and differs from that in inorganic semiconductors. Conducting polymers like PA can undergo both n-type (polymer reduction) and p-type (polymer oxidation) doping while, for example, in the case of PPy only p-type doping is possible. Due to a strong electron-phonon interaction in one-dimensional systems, quasi particles like polarons (radical-cation or radical-anion, with a single charge ±e and spin ½) [14] bipolarons (energetically more favourable, consisting of coupled two polarons and having integer spin,) [14] and, in the case of trans-polyacetylene also soliton (the neutral soliton carries no charge and still has spin ½; whereas the charged soliton is spinless) [15] are the charge carrier species found in conducting polymers [16]. Whereas, solitons can be found only in trans-polyacetylene, polarons and bipolarons are responsible for high conductivity in most of the doped conjugated polymers.

Additionally, the electrical, optical and electrochemical properties of some conjugated polymers, e.g. PANI or PPy, can be easily controlled by protonation via acid-base reactions. Recently, composites of conducting polymers with a large spectrum of organic (cellulose [17], gelatin [18], etc.) and inorganic clays [19,20], transition metal dichalcogenide [9,21], and metal oxides [22] fillers have been prepared and studied intensively as the way for further improving electrical and mechanical properties, as well

as their thermal stability and processability [23].

The great diversity of properties, like the environmental stability, mixed electronic and ionic conductivity, electroactivity, and biocompatibility have made conducting polymers suitable for a large variety of applications that include chemical and physical sensors [24,25], batteries [26], supercapacitors [27–29], solar cells [30], anti-corrosion coatings [31], membranes [32], ion-selective electrodes [33], electrochromic materials [34,35], memristors [36,37], organic thin-film transistors [38], tissue engineering [39,40], electromechanical actuators and many others.

1.1.1 Evolution of energy band structure

To understand the basic nature of electronic properties of conducting polymers, chemical bonding configuration has to be explored. Atomic orbital hybridization model can be used for these polymers where carbon is the main atom in the backbone. In most commodity polymers, all 2s, $2p_x$, $2p_y$ and $2p_z$ valence orbitals of carbon are involved in the hybridization and constitute the sp^3 hybridized orbital. In the case of sp hybridization, only two electrons per C atom, namely from 2s and $2p_x$ orbitals, are involved. These orbitals result in strong covalent bonds called σ bonds, which are highly directional along the polymer axis. Remaining $2p_y$ and $2p_z$ orbitals are not involved in the hybridization and form π bonds. They are orthogonal to the σ bonds and hinder rotation around the σ bond axis. In the case of sp^2 hybridization, three σ bonds are formed with neighbour atoms originated from the 2s, $2p_x$ and $2p_y$ orbitals, whereas the remaining $2p_z$ orbital forms the π bond. In the sp^3 hybridization, all the valence orbitals get involved to the hybridized orbital so that tetrahedral orientation of the σ bonds is formed. Molecules composed of carbon only with sp^3 hybridized orbitals have so called saturated bonds, whereas molecules with π bonds are unsaturated. Most of the conjugated polymers have an unsaturated backbone with one sp^2 hybridized and one p_z orbital per CH-group and the π bond is formed where the p_z electron wavefunctions of adjacent C atoms overlap. Within the molecular orbital theory, the π electrons occupy the π bonding orbital, which is the highest occupied molecular orbital (HOMO). The lowest unoccupied molecular orbital (LUMO) is the antibonding π* orbital (Fig. 2). HOMO and LUMO orbitals are equivalent to the valence and conduction bands of inorganic semiconductors. With the increasing number of atoms in the polymer chain each atomic energy level splits into many levels which depend on the number of interacting atoms, resulting in an energy band. Contrary to the crystals of inorganic semiconductors electrons are not delocalized over the whole polymer chain, the delocalization is limited over only a few repeat units of the polymer. The bandgap separating conduction and valence band has a very small density of states produced by structural imperfections and impurities. When these chains come together in a polymer with a weak interchain electronic coupling, the bands are stabilized to have smaller ionization potential and larger electron affinity by the screening effect.

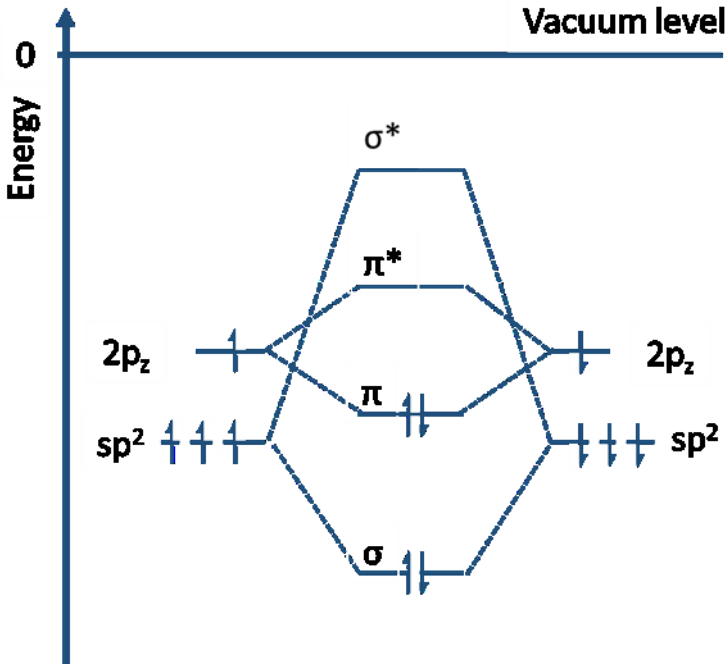

Figure 2: Energy splitting diagram of bonding and anti-bonding orbitals for ethene. Here, $2sp^2$ hybrid orbitals forming σ-bonds with hydrogen atoms are not shown for clarity. Adapted from ref [41].

1.1.2 Doping and free charge carriers

From the point of view of electronics, conducting polymers are semiconductors, some of them with a relatively wide bandgap that makes their properties in the neutral state closer to insulators. Hence, a doping is required to enhance their conductivity. When doped with an electron acceptor, electrons are removed from the delocalized π orbitals and holes are created as majority charges. The hole is delocalized over several monomer units of the polymer backbone, depending on mutual orientation of the carbon p_z orbitals that influences their transfer integrals. The charge transfer to a next delocalized segment proceeds via hopping mechanism that requires a certain amount of the reorganization energy of the molecule.

Besides the chemical doping, free charges can be created also by electrochemical doping, photodoping, or charge injection at a metal-semiconductor interface. It should be noted that the doping process in CPs is different compared to their inorganic counterparts. In inorganic semiconductors, dopants with number of valence electrons different from the atoms of the parent material replace some of the parent atoms in the crystal lattice making some electrons loosely bound. In polymers, there is a charge transfer between the polymer chain and a dopant, creating free charge carriers in the form of radical ions (polarons), dications or dianions (bipolarons) or charged solitons on the polymer backbone. The solitons represent actually defects in conjugation, which behave as a self-reinforcing solitary waves moving along the polymer backbone without dispersion. They are formed in CPs with the degenerate ground state, like in trans/isomer of polyacetylene, where two phases

of the electron wavefunction occur separated by the soliton defect. Polarons and bipolarons are formed in polymers possessing the non-degenerate ground state, which is the case in most of the conjugated polymers. In these polymers, doping causes cleavage of the double bonds, which leads to the distortion of the polymer chain 1-dimensional lattice. This change in geometric structure results in the transformation of low energy aromatic (benzoid) structure to energy-rich quinoidal structure. The benzoid structure has a higher ionization potential and a lower electron affinity than the quinoidal structure.

It has been reported that p-type doping is more stable than n-type doping. Upon oxidation π-electrons are removed from the HOMO level causing polarons formation. When the oxidation level is further increased more electrons are transferred from HOMO of the polymer to the dopant creating bipolarons as depicted in Fig. 3.

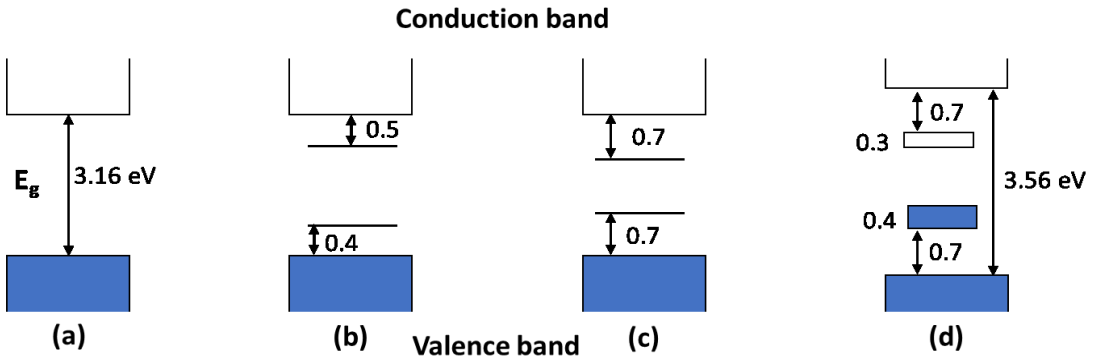

Figure 3: Illustration of the electronic band structure of PPY as a model material: (a) undoped polymer, (b) polaron (c) bipolaron and (d) bipolaron band formation in the fully doped polymer. Adapted from ref [42].

1.2 Charge transport models

Besides the concentration of free charges (n_c), the electrical conductivity (σ) depends also on the charge carrier mobility (μ_c), according to the formula $\sigma = n_c q_c \mu_c$, where q_c is the elementary charge. The limited delocalization of π-electrons caused by chain distortion and weak intermolecular interactions together with a distinct morphological and structural disorder in conjugated polymers, restricts the charge carrier transport. Instead of the Bloch wave that describes the charge transport of electron in a crystal of the inorganic semiconductor the charge moves by incoherent hopping between sites where it is localized for a period in about picosecond timescale. The "site" in conjugated polymers can be considered as consisting of several repeat units of the polymer.

In case of conducting polymers, the band model cannot explain sufficiently the charge transport mechanism because of limited delocalization of charges, weak intermolecular interactions and disordered nature of polymers. Charge transport in

amorphous polymers is largely dependent on the nature, density and mobility of available charge carriers, voids in the polymer, polymer chains entanglement, and also on the experimental conditions like applied electric field, temperature etc. The electronic states in CPs resemble those in inorganic amorphous semiconductors and can be roughly classified as extended states (with some delocalization) and localized states. In disordered systems, the wave function of an electron is limited to a small localization site (finite region) and decays exponentially with increasing distance unlike in crystalline materials where electron wave functions are thought of as Bloch waves as illustrated in Fig. 4. Anderson [43] laid out the foundation of the theory of charge transport in disordered materials, where localized states and the defects in the lattice are inherent. In this case, the localized electron wave function takes the form:

$$\varphi(\mathrm{r}) \; \alpha \; \exp\left(-\frac{r}{a}\right) \qquad (1)$$

where r is the position and a is the size of the localized state. It shows that charge transport occurs via tunnelling or hopping between these localized states which might be assisted by phonons. It is different from the band transport which is limited by scattering of moving charges on phonons. It is worth to point out the meaning of the position of the Fermi level (E_F). If E_F lies in the energy interval of localized states, the material shows non-metallic behaviour whereas if E_F lies in extended state region, metallic-like behaviour is observed with a finite DC conductivity as shown in Fig. 4:

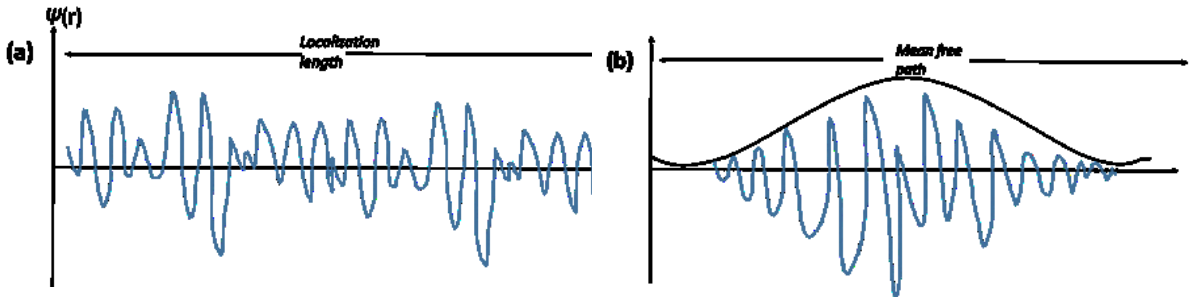

Figure 4: (a) Typical localised wave function with localization length (b) Extended Bloch wave function with mean free path. Adapted from ref [43].

Based on extended states and localized states, the charge transport mechanism can be divided into three groups:

a) *Transport via extended states*: Since the charge carriers are spread out, the mean free path becomes long enough and hence charges move as in the bandlike transport. In this case, charge carriers are only weakly scattered by smaller defects, impurities and can be considered as in nearly free approximation according to standard Fermi liquid approach and Boltzmann theory [44].

b) *Transport through localized states*: In this case charge transport occurs via hopping

mechanism between individual localized states. It has been described in detail in the section results and discussion 3.1.

c) *Transport involving both extended and localised states*: This mechanism is based on multiple trapping and releasing (MTR) model. When the charge carriers are in localised states, they become trapped and can further move only if they are thermally released back to the extended states where they are mobile until they are trapped again by another localized state. The boundary between extended and localized states is called "mobility edge" which looks like a transport band inside the band gap (Fig. 5).

It should be also noted that some localized energy levels can be so deep in energy that the charge release is limited. These levels form deep traps that influence the charge transport by a space charge formation.

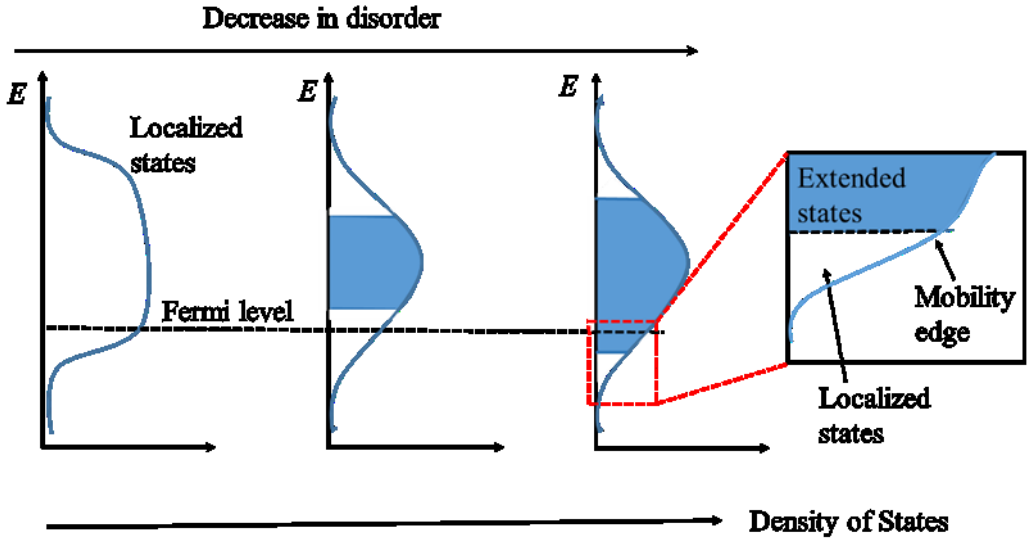

Figure 5: Illustration of localized, extended states and mobility edge in disordered systems. Adapted from ref [43].

1.2.1 Temperature dependence of DC conductivity

The measurements of temperature dependences of conductivity are of fundamental importance to determine the charge carrier transport mechanism. From the various models proposed in the literature, some models related to the research summarized in this work are presented below.

a. Metallic Regime of Quasi one-dimensional system: This model describes the highly doped CPs, where polymeric chains are well oriented with a high degree of regularity. It was first demonstrated on defect-free homogeneously doped polyacetylene chain, which can be regarded as a quasi 1D metal [45]. According to this model the conductivity depends on temperature as:

$$\sigma(T) = \sigma_0 \exp\left[\frac{h\upsilon_0}{k_B T}\right] \quad (2)$$

where $h\upsilon_0$ is energy of phonons responsible for back-scattering of electrons and σ_0 is the conductivity at the high temperature limit. Back scattering of electrons on phonons is a major limitation for charge transport according to this model.

b. Variable Range Hopping (VRH) model: The states below the Fermi energy level are occupied and the states above are empty except for those occupied by thermal excitations. The electrons hop from occupied to empty states. Depending on their mutual position of energy levels, they might need to hop upward in energy. Many phonons are available at high temperature that can assist upward hopping. The electrons have to find another energetically accessible state as the phonons freeze out at low temperature. Hence, the average hopping distance increases giving the name "Variable Range Hopping". The conductivity in this case decreases because of hopping becomes less probable [46] and is expressed as:

$$\sigma(T) = \sigma_0 \exp\left[-\frac{T_0}{T}\right]^{\gamma} \quad (3)$$

where σ_0 is the high temperature limit of the conductivity, T_0 is the Mott's characteristic temperature associated with the degree of localization of the electronic wave functions, and $\gamma = 1/(n+1)$, n being the dimension in which the charge transport takes place. It follows that $n = 1$ for one-dimensional hopping but, according to Efros and Shlovskii [47], $n = 1$ could arise also for 3D hopping if the electron-electron interaction is considered.

Epstein et al [48] has emphasized that quasi 1D hopping is prominent in conducting polymers where the chains traverse disordered regions interconnecting crystalline domains. The charge carriers diffuse along electrically isolated disordered chains and localize owing to the nature of the one-dimensional chain. In this case, 1-D VRH dominates the overall conductivity of polymer.

c. Charging Energy Limited Tunneling Model (CELT): This model developed by Sheng et al. [49] is used for the conductivity in granular systems, where it is controlled by tunneling between small conducting grains at low electric field providing the temperature dependence conductivity as:

$$\sigma(T) = \sigma_0 \exp[-\frac{C}{T^a}] \quad (4)$$

Here, C is a constant, and a=1/4 for T approaching zero temperature and it is greater than ½ but less than 1 at the high temperature limit. The temperature at which crossover occurs depends on the distribution of conducting grain sizes. The interpolation between these limiting values often results in the widely observed a = 1/2 behaviour over the intermediate temperature interval where most of the measurements are performed.

d. Fluctuation-Induced Tunneling Model (FIT): Originally developed by Sheng [50] for granular metals in insulating matrix, this model assumes that thermally activated voltage fluctuation modulates the barrier height between conducting domains. It considers either rectangular or parabolic tunneling barriers, and yields the expression for the conductivity:

$$\sigma(\mathrm{T}) = \sigma_0 \exp[-\frac{T_1}{(T - T_0)}] \quad (5)$$

Later, this model was extended to insulating barriers by introducing geometric factors for heterogeneous systems proposed by Kaiser et al [51]. Further, Conwell and Mizes [52]demonstrated that the presence of conjugation defects and chain breaks gives an increase of conductivity with temperature due to the absorption of phonon energy by charge carriers that become activated to cross the barrier. Baughman and Shachklette [53] revealed the impact of the conjugation length on the conductivity and found its exponential temperature dependence based on random resistor network model. Similarly, Roth [54] described the relationship between the conductivity, length of conjugation, and the exponential dependence of temperature.

e. Random Barrier Network model (RBN) model: This model relates to the percolation-type conductivity in a system having macroscopic inhomogenities. Sinkkonen [55] used effective medium theory [56] to analyze the percolation threshold of the thermally activated conductivity given by the expression:

$$\sigma(\mathrm{T}) = \sigma_0 \exp[-\frac{eV_0}{k_B T}] \quad (6)$$

where V_0 is the barrier height which determines the activation energy of the conductivity. Above the percolation threshold, the activation energy decreases with increasing temperature and with decreasing fraction of barriers. At very low temperatures, conductivity becomes temperature independent.

Inspecting the above models, a universal expression can be drawn for the temperature dependence of the conductivity to reflect all the above conducting mechanisms as:

$$\sigma(\mathrm{T}) = \sigma_0 \exp\left[-\frac{A}{\mathrm{T} - \mathrm{B}}\right]^{\gamma} \quad (7)$$

with different parameters for a particular model:
for FIT model, γ=1, A=T_1 and B=T_0; for VRH model, γ =1/2, 1/3, 1/4 for 1-, 2- and 3-D system, respectively, for CELT model, A=T_0 and B=0, γ being in the range of 1/4<n<1; and for RBN model, γ = 1, A = eV_0/k_B and B = 0.

Depending on the temperature range, different models could be applied since

different transport mechanisms can prevail.

a) *High temperature region*: Charges at localized states can be thermally excited to extended states lying above the mobility edge. At extended states, charges follow band-like transport model until they are trapped by another localized states as described above in the MTR model.

b) *Intermediate temperature region*: Since the energy difference between initial and final hopping states is comparable to the thermal energy k_BT, the charge transfer is energetically favourable unless the overlap integral of wavefunctions between these two states is negligible. Hence, the charge can hop round the Fermi level with available phonon energy. VRH is the dominant transport mechanism in this range.

c) *Low temperature region*: Since the thermal energy is much smaller compared to k_BT, the upward jumps are energetically unlikely. Hence, charge transfer is to the nearest neighbour which is spatial dependent. This is termed as 'nearest neighbour hopping'.

The metal-insulator transition property in CPs is particularly of the great interest because of the wide range of possible applications. By varying the disorder, the electrical properties can be easily tuned. Temperature dependence of conductivity gives insight to understand the transport properties in insulating, metallic and semiconducting type of polymers. As reported by Zabrodskii and Zinoveva [57], the temperature dependence of conductivity can be categorised into three distinct regimes based on the reduced activation energy (W) given by equation (8):

$$W(T) = \frac{d(\ln\sigma)}{d(\ln T)} \tag{8}$$

a) *Insulating regime:* Undoped or moderately doped CPs show insulating or semiconducting behaviour. The materials discussed in this thesis belong to this category. The charge transport is governed by the VRH model and it follows Mott's law as described in equation (3). The activation energy in this case has negative temperature coefficient since the conductivity is activated given by equation (9) [58] as :

$$logW(T) = A - xlogT \tag{9}$$

where $A = x\log T_0 + \log x$. By plotting *logW* vs *log T*, slope x can be easily predicted from the equation (9).

b) *Critical regime*: This is the boundary between metallic and insulating regime. The slope in equation (9) becomes zero since the activation energy is independent of temperature [59], and later Larkin and Khmelnitskii [60] showed that conductivity obeys a power law temperature dependence as:

$$\sigma(T) = AT^{\beta} \tag{10}$$

where A is a constant related to the correlation length and the exponent β is in the range of 0.33 to 1. It can be predicted that metallic sites dominate the transport if the value of β is bigger than 0.33 and insulating sites are limiting the conductivity if β approaches 1.

c) *Metallic regime*: This is applicable to heavily doped CPs which have highly oriented chains, and negligible disorders. The conductivity in this regime can be expressed as:

$$\sigma = \sigma_0 + mT^{1/2} + BT^{p/2} \tag{11}$$

where σ_0 is the conductivity at zero temperature, m is a diffusion coefficient, B is the correction to zero-temperature "metallic" conductivity and *p* is the scattering rate which takes the value 3/2, 2 and 3 for strong disordered materials, weak disordered materials and inelastic electron-electron scattering, respectively.

1.2.2 Charge transfer rate

In order to determine the charge transfer rates between two hopping sites in case of lightly doped polymers, two models, namely the Miller-Abrahams model [61] and polaron model expressed by semiclassical Marcus theory [62], are widely used. The transfer rates (υ_{ij}) between two sites, the initial (i) and final (j) ones, can be calculated within the Miller-Abrahams model as:

$$\upsilon_{ij} = \upsilon_0 e^{-2\alpha r_{ij}} e^{-\frac{\varepsilon_j - \varepsilon_i + |\varepsilon_j - \varepsilon_i|}{2kT}} \tag{12}$$

where, υ_0 is phonon vibrational frequency (also called as attempt-to-hop frequency), α is the inverse of localization radius called overlap factor, r_{ij} is the separation distance between two sites i and j, and ε_i and ε_j are their energy levels. The first exponential term shows the decrease in transfer rate with increasing distance between the sites while the second term is the Boltzmann factor related to the activation energy of the charge transfer process.

Within the polaron model, the hopping rate is given by the Marcus theory similar to Eq. (12) but with some modified meaning of the terms. It originates from the fact that polarization in the medium is caused by the residing charge, resulting in the lattice deformation. Hence, the charge transfer requires some reorganization energy bound to this deformation. For the electron transfer from the site A to the site B, the electron transfer reaction can be expressed as:

$A^- + B \rightarrow A + B^-$ (for the hole transfer $A^+ + B \rightarrow A + B^+$) as depicted in Fig. 6 [63].

The charge transfer rate can be then written as:

$$\upsilon_{ij} = \frac{|J_0|^2}{\hbar}\sqrt{\left(\frac{\pi}{\lambda kT}\right)} e^{-2\alpha r_{ij}} e^{-\frac{(\Delta\varepsilon_{ij}+\lambda)^2}{4\lambda kT}} \tag{13}$$

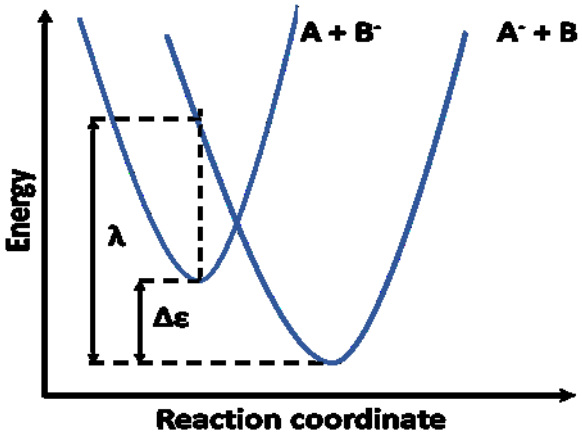

Figure 6: Potential energy surface for the charge (electron) transfer event.

where, J_0 is the electron transfer integral, ħ is the reduced Planck's constant, λ is the reorganization energy. The key point in this model is that the charge transfer rate does not keep continuously increasing with increasing energy difference because of the vibrational degrees of freedom. For a given reorganization energy λ and a negative driving force $-\lambda < \Delta\varepsilon_{ij} < 0$, the transfer rate at first increases (so called normal region), reaching the maximum at $\Delta\varepsilon_{ij} = -\lambda$ and then starts to decrease with $\Delta\varepsilon_{ij}$ turning even more negative. This region is called inverted region. It is to be noted that the inverted region is absent in Miller-Abrahams model.

It can be pointed out that both the expressions, Miller-Abraham and Marcus, are limiting cases of the time-dependent perturbation theory for weak electronic coupling. It is a general expression to calculate time-evolution of the system by expanding time-evolution interaction operator [64]. The Miller-Abraham formalism is valid for a weak electron-phonon coupling and at low temperatures while Marcus formalism is valid for a strong electron-phonon coupling and at higher temperatures. To include the effect of lowering the energy barrier by the applied electric field in both the formalisms, the additional term should be included as $\Delta\varepsilon_{ij} = \varepsilon_j - \varepsilon_i - q r_{ij}.E$, where q is the elementary charge, r_{ij} are the vector connecting the centres of two sites and E is the electric field vector.

1.2.3 Frequency dependent conductivity and modulus formalism

The frequency dependence of the complex AC conductivity, so called broadband impedance spectroscopy, gives an insight into the electrical properties of CPs arising from different conducting regions. If combined with the measurements of the temperature dependence of the conductivity, various interesting characteristics can be elucidated. At various frequency range the impedance is influenced by various effects like

molecular/dipolar fluctuations, polarizations at inner and outer boundaries, and charge transport. The alternating field causes a rotational motion of molecular dipoles and local translational motion of free charges. The DC conductivity is a limit of AC conductivity for frequency approaching zero. At very high frequency only the small mass entities like electrons can respond causing electronic polarization. Similarly, atomic and dipolar polarization occur at intermediate frequency range, whereas, ionic and space charge polarization are dominant at low frequencies.

The relationship between electric field E and current density j in the complex representation is given by:

$$j = \sigma^* E \tag{14}$$

Here, σ* is the complex conductivity expressed as:

$$\sigma^*(\omega) = \sigma'(\omega) + i\sigma^{"}(\omega) \tag{15}$$

where, σ′ and σ″ are the real and imaginary parts of the complex conductivity, respectively.

From the Maxwell's equations and time derivative of dielectric displacement, (D=ε*ε$_0$ E), σ′= ωε$_0$ε″(ω) and σ″ = ωε$_0$ε′(ω) hold. Here ε$_0$ is the dielectric permittivity of vacuum and ε′ and ε″ are the real and imaginary parts of the complex dielectric permittivity ε*. It can be deduced that if only the DC electronic conduction takes place the imaginary part of the complex permittivity ε″= $\frac{\sigma_{dc}}{\varepsilon_0 \omega}$ decreases linearly with increasing frequency with the slope= -1. At the same time, the real part ε′ remains to be constant if other polarization effects are absent. Here, σ$_{dc}$ is the DC conductivity and ω = 2πf is the angular frequency.

The analysis of the impedance spectra is often complicated by polarization effects like electrode polarization or polarization at boundaries of domains with different conductivity. To analyse the impedance spectra in these cases, a complex dielectric modulus formalism is often adopted, which supresses the effects arising from electrode polarization. It is defined as:

$$M^* = \frac{1}{\varepsilon^*} = \frac{1}{(\varepsilon - j\varepsilon^{"})} = M' + jM" = \frac{\varepsilon'}{(\varepsilon')^2 + (\varepsilon")^2} + j\frac{\varepsilon^{"}}{(\varepsilon')^2 + (\varepsilon")^2} \tag{16}$$

where, M′ and M′′ are the real and imaginary parts of the complex dielectric modulus (M*), respectively [65]. The DC conductivity can be then obtained as:

$$\sigma_{dc} = \frac{\varepsilon_0 \varepsilon_\infty}{< \tau >} \tag{17}$$

where τ is the relaxation time $\tau = \frac{2\pi}{\omega_{max}}$ is calculated from low angular frequency maximum ω$_{max}$ of the M′′ spectrum.

In case of CPs with metallic behaviour, the frequency dependence of conductivity can be described using Drude equation as:

$$\sigma(\omega) = \frac{Net}{m(1 + f^2t^2)} \tag{18}$$

where t, N, e and m are scattering time, charge carrier density, elementary charge and mass of charge carriers, respectively. It can be concluded from this equation that if $f^2t^2 \ll 1$, then the conductivity is independent on frequency [46].

For the case of non-crystalline semiconductors with the hopping transport among localized states near the Fermi level (E_F), Austin and Mott [46] proposed the frequency and temperature dependence of AC conductivity as:

$$\sigma_{ac} = \frac{1}{3}\pi e^2 k_B T[N(E_F)]^2 \alpha^{-5} \omega[\ln(\frac{\omega_0}{\omega})]^4 \tag{19}$$

where ω_0 (~10^{12} Hz) is the phonon frequency and $N(E_F)$ is the electron density within the range of Fermi energy (E_F). According to this model σ_{ac} follows the dependence $\sigma_{ac} \propto T\omega^s$ for the frequency range $10^2 < \omega < 10^8$ Hz [46].

For disordered materials, the AC ionic and electronic conduction can be described by random barrier free energy model developed by Dyre [66], which assumes that hopping of charge carriers is subjected to spatially randomly varying barriers as depicted in Fig. 7. When solved within Continuous-Time-Random Walk (CTRW) approximation [67], the complex conductivity is obtained as:

$$\sigma^*(\omega) = \sigma_{dc} \frac{i\omega\tau_e}{\ln(1 + i\omega\tau_e)} \tag{20}$$

where, τ_e is the attempt to hop frequency to overcome the largest barrier determining the DC conductivity.

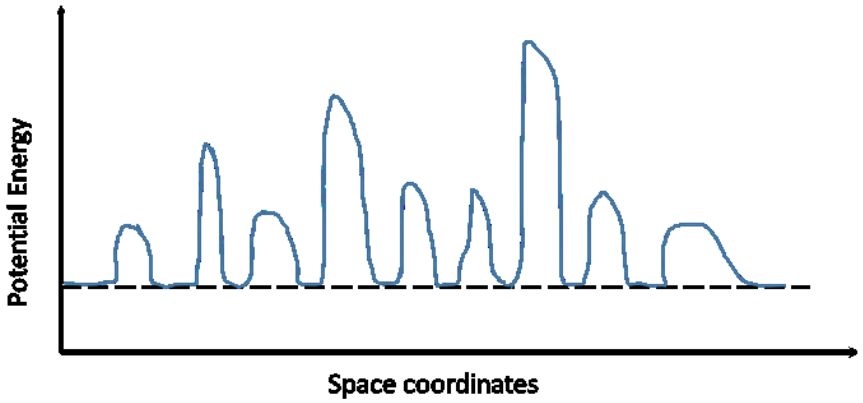

Figure 7: Hopping conduction subjected to a spatially randomly varying energy barrier.

Kohlrausch-Williams-Watts (KWW) model and Cole/Davidson model have been used extensively to analyse complex conductivity in glasses and melts with large concentrations of mobile ions but failing to describe the course of the conductivity in a broad frequency range specifically predicting incorrect relaxational behaviour at low frequencies [68].

Jonscher [69] proposed the frequency dependence of the real part of complex conductivity for a wide range of solids in a unified approach as:

$$\sigma' = \sigma_{dc} + A\omega^s \tag{21}$$

where, σ_{dc} is obtained by extrapolating σ' to the low frequency limit. The term $A\omega^s$ is the dispersive component of AC conductivity and it represents the degree of interaction between the lattices and mobile ions. *A* is the pre-exponential factor which is related to the polarizability, and *s* is a power law exponent, $0 < s < 1$, describing the electrical relaxation behaviour of the material. The dependence of *s* on temperature gives the information on the conduction mechanism [70]. Various models are proposed in the literature to give an insight to the predominant conduction mechanisms depending on the shape of the temperature dependence of exponent *s* at lower temperatures. If *s* increases with increasing temperature, a small polaron conduction mechanism can be expected, whereas if *s* decreases with increasing temperature, so-called correlated barrier hopping (CBH) takes place. If *s* remains independent on temperature, then quantum mechanical tunneling has been suggested [71].

The frequency dependence according to the CBH model, where the conduction occurs by polaron or bipolaron hopping over the Coulomb barrier separating two defect centres, can be expressed by equation (22):

$$s = 1 - \frac{6k_BT}{[W_M - k_BTln(1/\omega\tau_0)]} \tag{22}$$

where, W_M is the polaron binding energy, τ_0 is the characteristic relaxation time and k_B is the Boltzmann's constant. For large W_M/k_BT, the polaron binding energy can be easily determined as [72]:

$$W_M = \frac{6k_BT}{1-s} \tag{23}$$

1.3 Metallo-supramolecular polymers

Supramolecular polymers are the special category of polymers that are held together by coordinate covalent bonds or noncovalent bonds. Metallo-supramolecular polymers (MSPs) include metal species and the polymer backbone consists coordinate covalent bonds [73]. MSPs, formed by the complexation of π-conjugated organic ligands with chelate end-groups (dubbed unimers) to metal ions, have gained immense interest in recently. By the application of electrochemical potential, the redox activity of metal ions changes the energy structure of the metal complex in the polymer.

1.3.1 Electronic structure of metallo-supramolecular polymers

MSPs show various transitions like metal to ligand charge transfer (MLCT), ligand to metal charge transfer (LMCT), d-d*transitions of metal (d-f* transition in case of lanthanides) in addition to π-π* electronic transitions, where the energy band gap is inversely proportional to the effective length of π-conjugation [74]. These transitions make MSPs highly efficient in various electronic and optical applications, and particularly in electrochromic devices (ECD). In addition, the reversible coordination linkage gives benefits of solution processability arising from the dissociation of polymeric form existing in solid-state to oligomeric fragments in a solution [74].

Various metal ions such as Fe(II) [75], Ru(II) [76], Co(II) [74], Zn(II) [77], Eu(II) [78], Cu(II) [79], Os(II) [80] have been used to prepare MSPs materials for ECDs having different colors, related to various transitions. For example, MSPs with Co(II) show a weak d-d* transition, those with Zn(II) show an intraligand transition. The MSPs with Fe(II) ions show an intense, as compared to Co(II) and Ru(II), MLCT absorption band and reversible switching between different oxidation states because of the involvement of valence electrons, which can be easily altered during oxidation or reduction. Fe(II) ions have six coordination sites, which help to stable complexation with the bis(2,2′:6′,2″-terpyridin-4′-yl end-group) unimers [81]. The change in colour is achieved by changing the oxidation state of Fe ion; for Fe(II) the MLCT transition of d electron from the highest energy level (HOMO) to π* of unimers (LUMO) occurs (Fig. 8). When oxidized to Fe(III) MLCT band disappears [74].

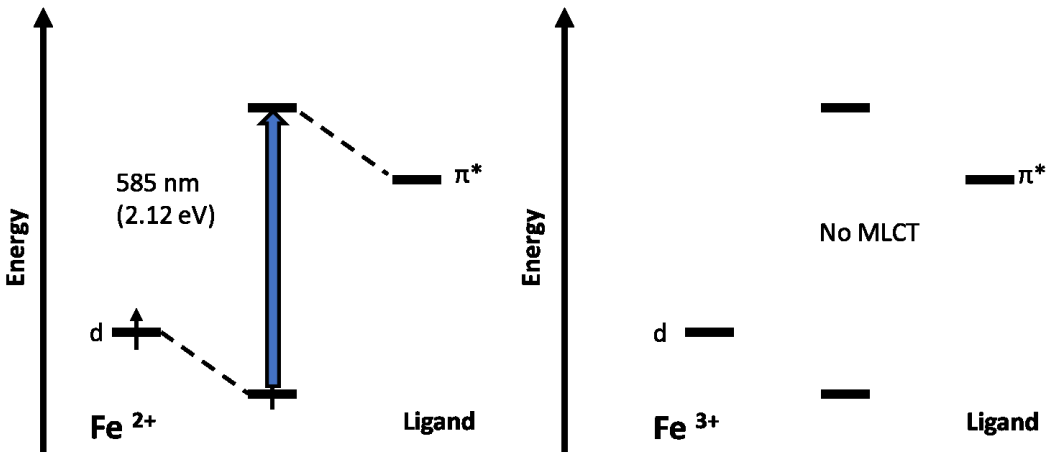

Figure 8. Energy diagram of Fe-MSP and its MLCT transitions. Adopted from [74].

In this thesis, the Fe-MSPs built with unimers based on thieno[3,2-b]thiophene central unit and various linkers (none, ethynediyl, 1,4-phenylene, and 2,2′-bithophene-5,5′-diyl) end-caped with bis(2,2′:6′,2″-terpyridin-4′-yl end-groups, denoted as Fe-Tt, Fe-Tte, Fe-TtPh and Fe-TtB, respectively, were characterized to elucidate the effect of chemical structure of the linker on their electrochromic properties.

1.3.2 Electrochromism

Electrochromism (EC) is a phenomenon in which a material changes color or opacity upon an electrical stimulus. This change should be persistent, it should remain after the stimulus is ceased and be possibly reversible. The nature of the color change is correlated to the change of the oxidation level of atomic or molecular species by redox reaction. The color change may occur between two colored states, or a transparent state ("bleached" state) and a colored state. Although known already since 1704, when the electro-coloration of Prussian blue (hexacyanoferrate), changing color from transparent to blue upon oxidation, was described by Diesbach, the real start of EC technology is attributed to S. K. Deb who described the coloration mechanism in WO_3 [82]. Many inorganic and organic EC materials [83] have gained a significant scope for a variety of energy saving and colour- or optical transparency-tuning applications. Both organic and inorganic EC materials have their respective advantages due to their other properties, like mechanical flexibility, spectral range, switching rate etc. Inorganic materials can work in the wide temperature range and possess good electrochemical and chemical stability whereas the organic ones can be easily modified to obtain targeted properties, showing rich colour, good processability and low cost. Transition metal oxides [84], hexacyanometallates [85], viologens [86], conjugated polymers [34,87–89], metallo–supramolecular polymers (MSP) [90], metal–organic framework [91,92], covalent organic frameworks [93], MXenes [94] have been explored for diverse emerging applications like smart windows [95], camouflage objects [81], optical switching devices [85], robotics [96], smart textiles [97], rare-view mirrors [98], electrochromic batteries [99], supercapacitors [100,101], or self-powered electrochromic windows [102]. Some of the EC materials and examples of their applications are summarized in Table 1.

Table 1. Electrochromic materials and their applications.

EC	Realized applications	References
WO_3	Smart windows	[95]
Chalcogenoviologen-based ionic liquids	Smart windows, E-price tag, flexible display	[103]
Polypyrrole	Self-rechargeable electrochromic battery	[104]
Poly(chalcogenoviologen)s	Flexible electrochromic battery	[105]
Zn@Ni@AgNFs//polyaniline	Flexible electrochromic Zn-ion battery	[106]
Potassium iron hexacyanoferrate dye (Prussian Blue)	Electrochromic optical switch	[85]
Polyaniline	Electrochromic E-skin	[96,107]
Poly(3,4-alkylenedioxythiophene)	Electrochromic displays	[108]
Polymers based on dioxythiophenes	Electrochromic eyewear (sunglasses)	[109]
Poly(1H-thieno[3,4-d]imidazol-2(3H)-one) derivatives	Electrochromic E-Paper	[110]
ZIF-67 (zeolitic imidazolate framework-67, or 2-methylimidazole cobalt salt)	Self-bleaching electrochromic mirror	[111]

It follows from Table 1, that during last decades polymer materials have been exploited in EC technology. The typical EC device (ECD) consists of a multilayer electrochemical cell composed of the following components [112]:

- Working and counter electrodes, at least one of them should be optically

transparent. Indium tin oxide (ITO) or more stable fluorine doped tin oxide (FTO) are the most commonly used to serve for this purpose.

- Layer of EC material. In some ECD two layers are used, each of them deposited on one electrode.

- Electrolyte layer. The electrolyte can be liquid (in this case sealing the ECD on the edges is required to prevent electrolyte leakage), gel or solid. Such electrolyte must be easily processable, facilitate charge transfer and chemically stable with regards to other materials in ECD. Poly(ethylene glycol) is used often as a solid electrolyte [113]. In addition to competitive electrochemical redox properties and optical properties of ECD, also the efficient charge transport in gel electrolyte is equally important to achieve high performance of the ECD. This gel electrolyte has a crucial role to balance the charge during the redox processes by transporting ions between the two electrodes. Fast gelation, rich ionic conductivity, low electronic conductivity (ideal zero), high transmissivity, electrochemical and thermal stability are some of the pre-requisites for a gel electrolyte to be used in ECD.

The ECD can operate in transmittance (most common, used for example in smart windows) or reflective mode (one of the conductive layers is replaced with a reflective surface like aluminium or silver; mostly used in car rear-view mirrors as shown in Fig. 8.

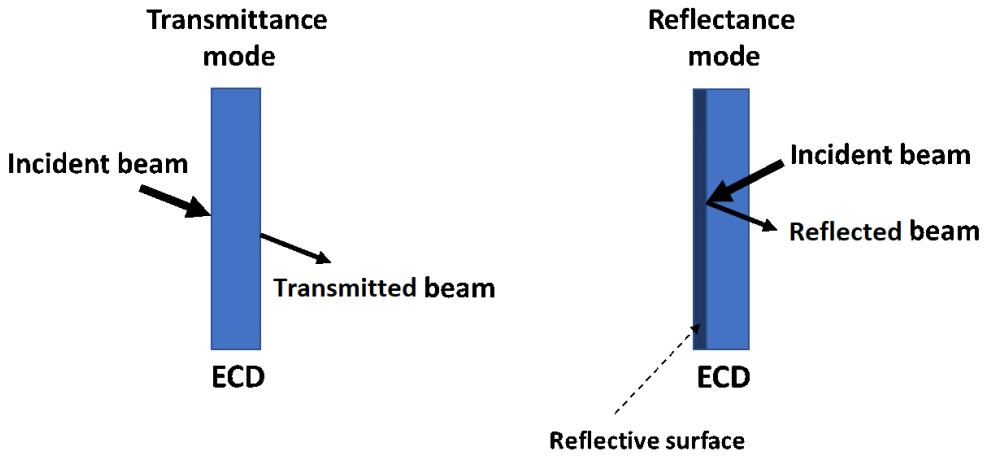

Figure 9. Modes of ECD operation

Under the applied voltage, the active material in EC devices undergoes a redox reaction. By changing its oxidation state, its optical absorption spectrum changes. Hence, an efficient charge transfer process at the active layer/electrolyte interface is crucial for the high performance of this system.

Coloration efficiency CE = $\frac{\Delta OD}{Q}$, defined as a ration of the change in the optical density ΔOD to the charge Q injected/ejected per unit area of the electrochromic layer

causing this change, is an important parameter of the ECD since the supplied charge is related to the electrical power required for electrochromic switching. The change in the optical density is defined as ΔOD = log (T_b/T_c), where T_b and T_c refer to transmittance in bleached and colored states of the EC film, respectively. The change in the optical density is usually related to the maximum in the absorption spectrum of the active material.

For high coloration efficiency, a maximum absorbance change achieved with minimum electrical energy is required. This parameter can be affected by various factors like the film deposition process, thickness of the layer, electrolyte interactions, doping level, potential windows of the particular application, redox activity of the material.

The switching time is also an important parameter which accounts for the time required to color or bleach. Bleaching and coloring times are usually reported as the time taken to reach 95% of final transmittance at a given wavelength. The fastest the response time, the better is the performance of ECD. For smart windows the switching time can be longer [95], however for displays the fast response is crucial and should be in a millisecond scale [114].

In an ECD, the current (I) inducing the change in color is given by equation (24) [115]:

$$I = \frac{V_e}{R_t} = \frac{[V_a - (\varphi_{IS} - \varphi_{EC}) - V_b]}{R_t} \tag{24}$$

where, V_e is effective colouring voltage, V_a is the applied voltage, V_b is the sum of all interface potential barriers, R_t is the sum of the total resistances composed of the electronic resistance of the active layer and the resistance given by ionic conductivity of the electrolyte and φ_{IS} and φ_{EC} are the internal chemical potential differences of ion storage layers and EC layers, respectively. The effective colouring voltage and the total resistances depend on the chemical structure of the electrochromic layer and its thickness, thickness of ion storage layer, ion concentration and their mobility. For the optimal EC performance higher voltage than V_e should be applied to overcome the barrier potentials in the system but overpotential should be avoided to limit chemical degradation and irreversible side reactions of the components of ECD.

From the point of view of EC applications, the ideal ECD should possess high optical contrast and electrochromic coloration efficiency, short switching time, and good environmental and redox stability. As mentioned above, large variety of inorganic and organic materials are known to be utilized in ECD, however, they still suffer from several disadvantages, e.g., limited color variation in case of inorganic or poor stability in case of organic materials. Recently, the promising EC materials, metallo-supramolecular polymers (MSPs), formed by the complexation of π-conjugated organic ligands with chelate end-groups (dubbed unimers) to metal ions, have gained immense interest.

2. Experimental and characterization techniques

2.1 DC Conductivity

Four probe method was used for the DC conductivity measurements in order to eliminate the contact resistance that could markedly influence the conductivity values obtained for our mostly highly conducting polymers. Two different electrode configurations were used depending on the material under study: Van der Pauw method for pellets made of powder of not film forming polymers, and linear electrode arrangement for free standing films. Low resistance contacts were employed to eliminate possible erroneous results caused by heating. The error originated in a self-induced voltage offset within the circuit was corrected by measurements with reversed applied voltage.

Van der Pauw method was employed to measure the conductivity of the powder materials in the form of pressed pellets. The pellets were prepared from a powder dried over silica gel at room temperature until reaching a constant weight, using a hydraulic press Trystom H-62 (Trystom, Czech Republic) under pressure 530 MPa. The diameter of the pellets was 13 mm and typical thickness around 1 mm. For the measurements, the pellets were inserted in a home-made sample holder equipped with four gold plated spring-loaded electrodes that made equidistant contacts at the perimeter of the pellet (Fig. 10). A Keithley 230 programmable voltage source in a serial connection with a Keithley 196 System DMM served as a current source and the potential difference between the potential probes was measured using a Keithley 181 Nanovoltmeter (Keithley, USA). Measurements were carried out in two perpendicular directions at stable ambient conditions at temperature 23 ± 1 °C and relative humidity 35 ± 5 %. The current was kept below 1 mA to avoid heat dissipation in the sample. For temperature dependence of DC electrical conductivity, the above process was repeated at different temperatures. The temperature was controlled by Quatro power supply in a sample chamber of the Broadband Impedance Spectrometer (Novocontrol Technologies, Germany) in nitrogen atmosphere.

The resistance *R* was determined as an average value of the resistances obtained in two perpendicular directions, horizontal (R_h) and vertical (R_v), which were calculated from the slopes of the linear part of the current-voltage characteristics measured in the respective direction. The bulk conductivity σ was calculated as [116]:

$$\sigma = \frac{ln(2)}{\pi d R} f\left(\frac{R_v}{R_h}\right) \tag{25}$$

where, d is the thickness of the sample, and the correction function *f* was taken from the van der Pauw equation [117] as:

$$e^{-\pi d R_v \sigma} + e^{-\pi d R_h \sigma} = 1 \qquad (26)$$

Since the ratio of the resistances measured in two directions was usually close to 1 and the samples were of circular shape with equidistant contacts symmetrically located along the perimeter, the correction factor f = 1 was taken in most cases.

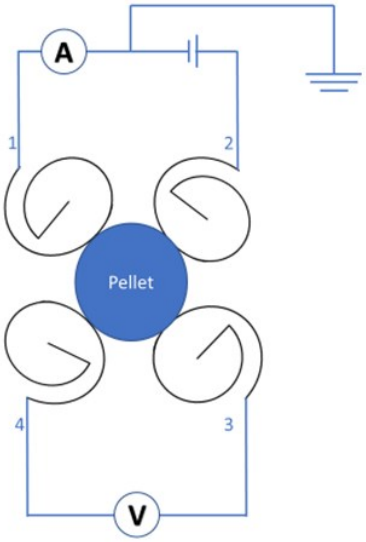

Figure 10: Schematic diagram of the experimental arrangement for the conductivity measurement using van der Pauw method.

Linear four probe method was used to measure the conductivity of free-standing films and thin films cast on a substrate. It involved four equally spaced spring-loaded probes, the outer ones used as current probes whereas the inner two electrodes were used to measure the potential difference (Fig. 11).

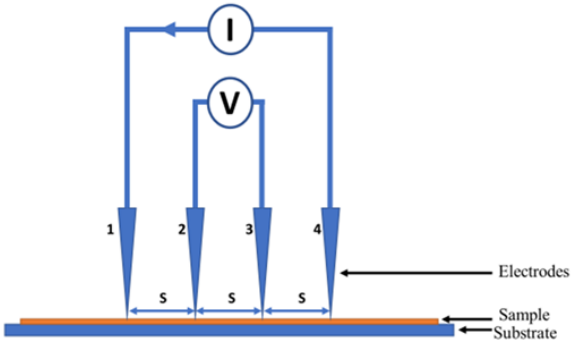

Figure 11: Schematic diagram of the conductivity measurement of thin film using linear four probe method.

The conductivity σ was calculated from the resistance R obtained from the slope of the current-voltage characteristics as:

$$\sigma = \frac{1}{2\pi sFR} \tag{27}$$

where, F is a correction factor and s is the probe spacing. The thicknesses t was typically hundreds of micrometers, appreciably smaller than the probe spacing (1.42 mm). Hence, correction factor (F) was used given by equation (28) [118] which is also valid for the films cast on non-conducting bottom substrate.

$$F = \frac{\frac{t}{s}}{2ln\left(\frac{sinh\left(\frac{t}{s}\right)}{sinh\left(\frac{t}{2s}\right)}\right)} \tag{28}$$

For thin samples, using the approximation $sinh(x) = x$ for $x \ll 1$, equation (27) reduces to:

$$\sigma = \frac{1}{4.53tR} \tag{29}$$

2.2 Broadband Impedance Spectroscopy

Broadband impedance spectroscopy was another experimental technique used in this thesis to better elucidate the conduction mechanism. The impedance measurements in the frequency range 10^{-2} to 10^{9} Hz enabled to distinguish charge transport and polarization effects at inner and outer boundaries, and dipolar and molecular fluctuations. The data were analyzed according to the equations (15- 24) described in the section 1.2.3. Frequency dependent conductivity and modulus formalism.

For the measurements of frequency and temperature dependences of the impedance, ~50 nm gold electrodes were deposited on both sides of the pellets by vacuum deposition. The experimental setup is depicted in Fig. 12. The samples were placed in the sample holder between the gold-plated brass disk electrodes 13 mm in diameter. The temperature dependences of the impedance spectra were measured in a quasi-steady-state regime using an Alpha-A Analyzer and Quatro Power Supply temperature controller (Novocontrol Technologies, Germany) under applied AC voltage 1 V_{rms} in the frequency range 10^{7} to 10^{-2} Hz and temperature range 115 to 435 K with 20 K step in nitrogen atmosphere. The calculations were done as described in section 1.2.3 using equations (14-24).

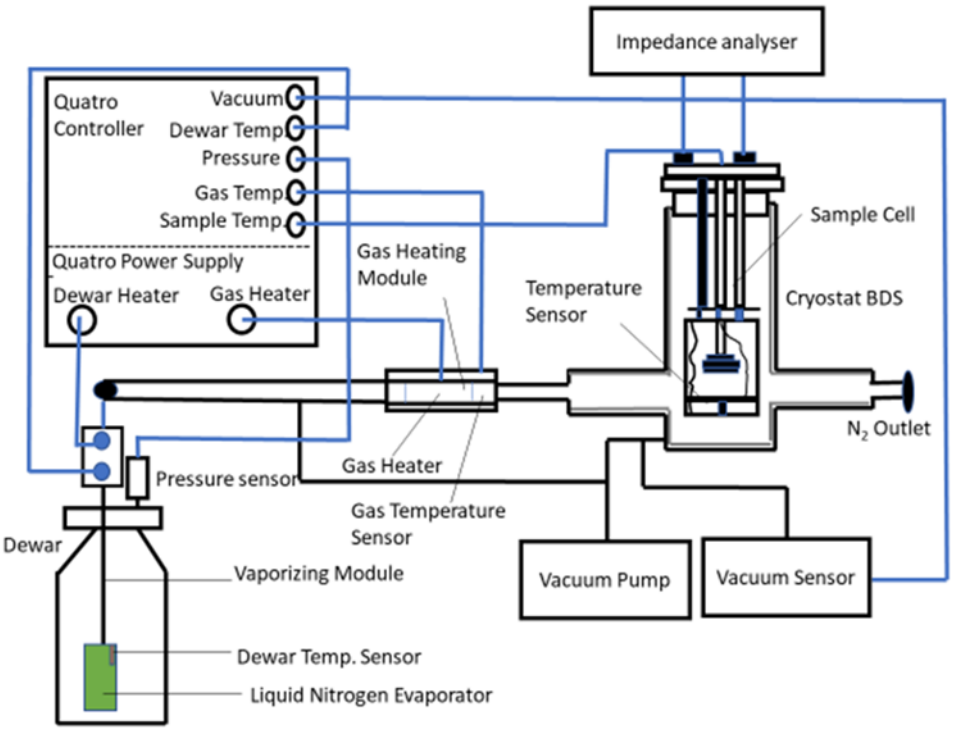

Figure 12: Experimental setup for the temperature-dependent broadband impedance spectroscopy.

2.3 Spectro-electrochemical characterization

Spectro-electrochemical and electrochemical kinetic studies were performed using UV-vis-NIR Lambda 950 spectrometer (Perkin Elmer, UK) in combination with Bio-logic potentiostat/galvanostat VSP300 as shown in Fig. 13. For the electrochemical characterization, three-electrodes setup was used and evaluated using the equation (24). Fe-MSPs films were spin cast on ITO glass which worked as working electrode, a platinum wire as a counter electrode and Ag/Ag+ wire was used as a pseudo-reference electrode. The measurements were performed in 0.1M acetonitrile (ACN) solution of tetrabutylammonium hexaflurophosphate (NBu_4PF_6) in a quartz cuvette (1 cm) at room temperature. All the potentials are reported versus the Ag/Ag+ pseudo-reference electrode. The optical response of ECD was assessed with spectrophotometer equipped with an integrating sphere.

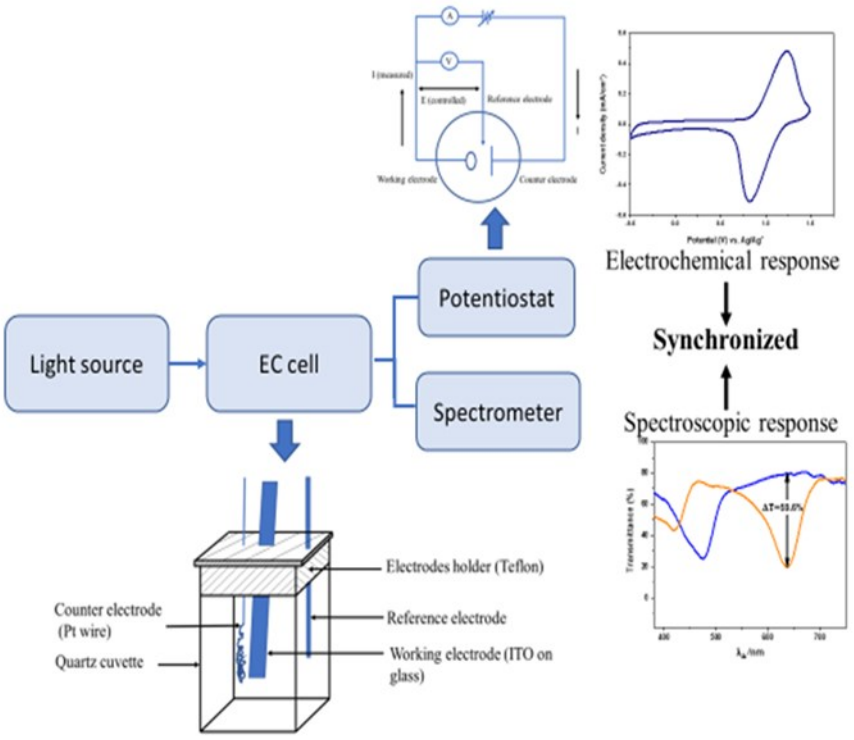

Figure 13. Experimental set-up for spectro-electrochemical measurements.

2.4 Other techniques

- *Electron Microscopy*: The morphology of all the investigated materials was studied with scanning electron microscopy (SEM) using a JEOL 6400 or VEGA Tescan microscope and/or with a transmission electron microscope (TEM) JEM 2000 FX or TECNAI G2 SPIRIT microscope. Additionally, the TEM was used to confirm the coating of MoS_2 surface by PPy.

- *Vibrational spectroscopy*: Fourier-transform infrared (FTIR) and RAMAN spectroscopy were used to identify the molecular components of the synthesized materials, their structures and, in the case of PPy synthesized in the presence of dyes, also the intermolecular interactions. FTIR spectra of the powders dispersed in potassium bromide pellets were recorded in the transmission mode using a Thermo Nicolet NEXUS 870 FTIR Spectrometer (Nicolet, USA) with a DTGS TEC detector in the wavenumber range 400–4000 cm^{-1}. Obtained spectra were corrected for the presence of moisture and carbondioxide in the optical path. Raman spectra were recorded with a Renishaw InVia Reflex Raman microspectrometer (Renishaw, UK). The spectra were excited with argon-ion laser emitting at 514 nm, HeNe laser emitting at 633 nm, and/or NIR diode laser emitting at 785 nm.

- *Surface area*: The specific surface area of the samples was determined using Gemini

VII 2390 (Micromiretics, Instruments Corp, Norcross, USA) or Autosorb-iQ (Anton Paar QuantaTec Inc.) with nitrogen as a sorbate at 77 K. 40–50 mg of the samples was outgassed in vacuum at elevated temperature. The specific surface area of the samples was calculated using the Brunauer–Emmett–Teller (BET) method.

- *Thermogravimetric analysis (TGA)*: TGA of the composite materials was carried out on a Perkin Elmer Pyris 1 (Perkin Elmer,Waltham, MA, USA) in the temperature range 35 –800 °C at the rate 10 °C min^{-1} with fixed air flow rate at 25 mL min^{-1}. This technique was mainly used to evaluate the amount of inorganic material (MMT) in the composites.

- *X-ray powder diffraction (XRD)*: This measurement was used to evaluate exfoliation during the in-situ polymerization or to study the intercalation process. It was performed using a pinhole camera (MolMet, Rigaku, Tokyo, Japan, upgraded by SAXSLAB/Xenocs) attached to a micro-focused X-ray beam generator (Rigaku MicroMax 003) operating at 0.6 mA and 50 kV. The camera was equipped with a vacuum version of the Pilatus 300 K detector.

- *Atomic force microscopy (AFM)*: Surface topography and roughness of the deposited films was studied in air using a Nanoscope IIIa (Veeco Instruments New York, NY, USA) atomic force microscope operating in the tapping mode (OTESPA-R3, Bruker silicon tips with spring constant of k = 26 N m^{-1} and resonance frequency of 300 kHz).

- *Profilometry*: Alongside AFM, profilometer was also a useful technique to assess the surface roughness and thickness of the film. The films were scratched to make a trench and then the height profile was measured using a KLA Tencor P-10 Profilometer.

- *Contact angle measurement*: This technique was used to determine the surface energy of the films. The static water contact angle of sessile drop (3 μL) was measured by a contact angle goniometer OCA 20 (Dataphysics, Germany) equipped with SCA 21 software where the profile was fitted with the Young–Laplace equation. At least three measurements were done at different position of each samples and average value is reported.

3. Results and discussion

3.1 Conductivity of conducting polymers and charge transport mechanism

Conducting polymers and their composites are favourable candidates for energy related and electronic applications, however, understanding final properties like conductivity and charge transport mechanism is crucial for further development. Therefore, this chapter focuses on the charge transport mechanism as a limiting factor of conductivity, and on elucidating the influence of the chemical structure and of the polymer morphology on the mobility of charges in the polymers and their composites.

3.1.1 Polypyrrole–molybdenum disulfide composites

Series of polypyrrole–molybdenum disulfide (PPy-MoS_2) composites were obtained by a single step *in-situ* chemical polymerization of pyrrole in the presence of micrometer-sized MoS_2 flakes, and their fundamental properties, mostly charge-carrier transport, were investigated **[Attachment 1]**. The variation of pyrrole to MoS_2 ratio during polymerization allowed preparing composites with tunable DC conductivity from 5 to 13 S cm^{-1}. The differences in the conductivity of these composites were assigned to different morphology of the PPy film formed at the surface of MoS_2 flakes (Fig. 14). At the low pyrrole content in the reaction mixture used for the composite preparation, relatively smooth PPy film on the MoS_2 surface was formed with a thickness around 30 nm (Fig. 14 a). Increasing the pyrrole amount led to thicker coating (thickness 100 to 140 nm) with clearly visible secondary growth of PPy particles (Fig. 14 b). The formation of PPy as well as its structure were confirmed by FTIR and Raman spectroscopy. The presence of exfoliated MoS_2 layers was confirmed but no PPy intercalating MoS_2 flakes was observed using wide-angle X-ray diffraction.

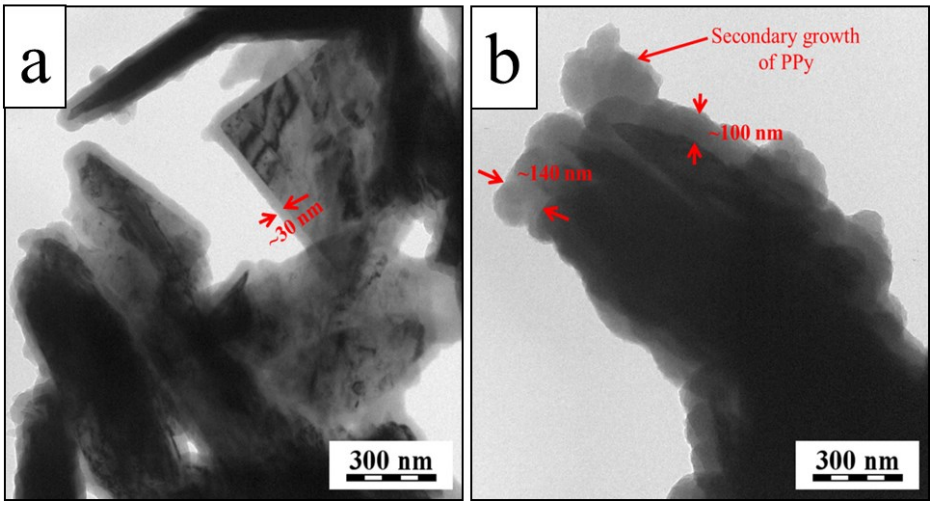

Figure 14. Transmission electron micrographs of PPy-MoS_2 composites with 15 wt% (a) and 45 wt% of PPy (b). The arrows indicate the PPy coating. **[Attachment 1]**

PPy-MoS_2 composites possessed substantially higher DC conductivity (Fig. 15) compared to the neat MoS_2 flakes (10^{-6} S cm^{-1}) and PPy globular (1 S cm^{-1}). A similar effect, but much less expressed, was reported previously on polyaniline/MoS_2 composites [119], where two-steps preparation procedure (exfoliation of MoS_2, followed by aniline polymerization) was used. In these composites, the increase of DC conductivity was explained based on interactions between polyaniline and MoS_2. In our case, the synergistic effect was assigned to the formation of well-ordered thin PPy film (Fig. 14a) at the MoS_2 surface, favourable for the efficient charge transfer. At low content of PPy in the composite more compact and non-porous PPy shell on MoS_2 flakes was formed because MoS_2 surface acts as a template for PPy chain growth from adsorbed oligomeric nucleates. In the case of higher PPy content, a secondary growth of PPy globules occurred on the PPy film previously grown on MoS_2 (Fig. 14b). The composites with these secondary grown PPy globules are less conducting due to a poor electrical connection between disordered globular boundaries. The better packed PPy shell at lower PPy content was also confirmed by BET measurement. The PPy-MoS_2 composite with the highest DC conductivity (13 S cm^{-1}) showed the specific surface area of 2.84 m^2 g^{-1}, while neat globular PPy and MoS_2 had the specific surface area higher, 26 and 13 m^2g^{-1}, respectively (Fig. 15.).

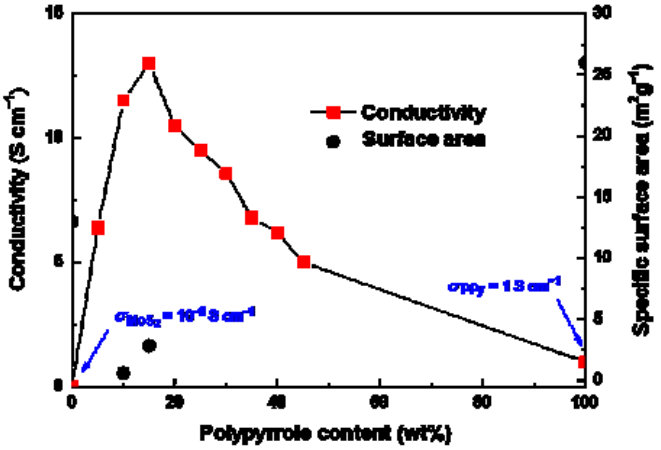

Figure 15. Dependence of the conductivity and the specific surface area of PPy-MoS_2 composites on PPy content. **[Attachment 1]**

Temperature dependence of DC conductivity measured in the interval from 130 to 400 K was employed to investigate the charge transport mechanism in the neat components and in the PPy-MoS_2 composites. In the case of disordered semiconducting materials, the electrical conductivity is typically assessed within a Mott theory given by Equation (3).

In the case of neat MoS_2 the temperature dependence of conductivity can be well fitted by a straight line in log (σ) *vs.* $T^{-1/2}$ plot (Fig. 16 a), which suggests that the transport proceeds via the one-dimensional hopping mechanism. Additionally, AC conductivity was only weakly dependent on temperature at high frequency range suggesting that the bulk of MoS_2 is not homogeneous (Fig. 16 b). At low frequency range below 10^3 Hz, the conductivity approaches a constant value indicating that MoS_2 is composed of small relatively compact grains which limits the long-range transport of charges. For the neat PPy the dependence of the DC conductivity on temperature revealed the Mott three-dimensional variable-range hopping (Fig. 16 c). The steep decrease of conductivity above 410 K from ~ 2 down to ~ 10^{-2} S cm^{-1} occurred due to partial deprotonation of PPy salt followed by conversion to less conducting PPy base [120]. For the PPy-MoS_2 composites, the data of DC conductivity (Fig. 16 d) follow the same trend and a log $\sigma \sim T^{-1/4}$ was found corresponding to the three-dimensional variable-range hopping charge transport mechanism but with different values of activation energy compared to the neat PPy. The electrical properties of the composites were found to be stable at much higher temperature compared to the neat PPy. No decrease of the conductivity was found at temperatures up to 150 °C.

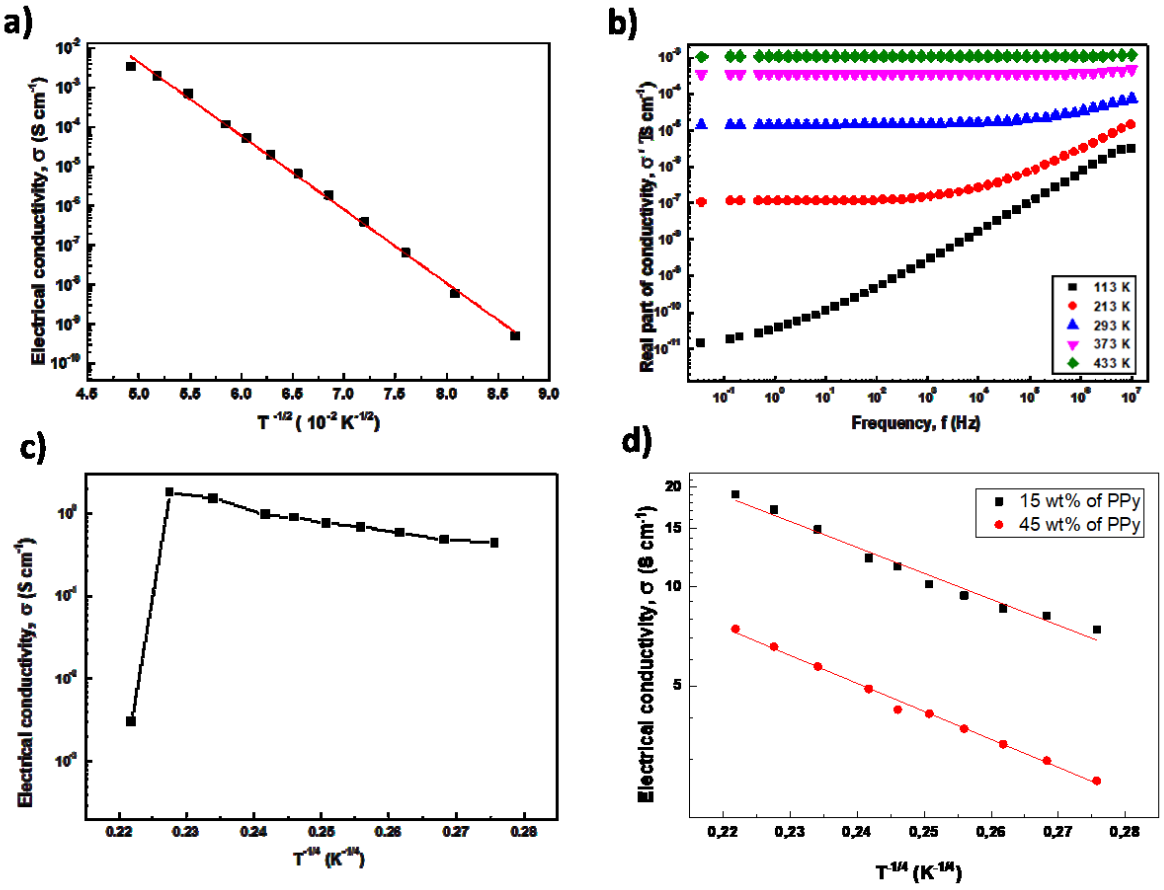

Figure 16. Dependence of the electrical conductivity, σ, of the neat MoS_2 on $T^{-1/2}$ (a); frequency spectrum of the real part of conductivity of the neat MoS_2 at various temperatures (b); temperature dependence of the DC conductivity σ of PPy (c), and of PPy/MoS_2 composites (d) as a function of $T^{-1/4}$.

3.1.2 1-D polypyrrole nanostructures

The enhancement of electrical conductivity of conducting polymers is one of the major requirements for many applications in soft electronics. Recently, it has been shown that the organization of PPy chains in one-dimensional structure leads to significant improvement of its conductivity. For example, when PPy was prepared in the presence of methyl orange, an anionic dye acting as structure-guiding agent, the morphology converted from typical globular one to nanotubes, and the conductivity increased about hundred times, from 1 S cm^{-1} to 100 S cm^{-1} [121]. Based on the knowledge of the impact of the dye on the properties of PPy, we selected two anionic dyes, Acid Blue 25 and Acid Blue 129 **[Attachment 2]**, and two cationic dyes, safranine and phenosafranin **[Attachment 3]**, as additives to the pyrrole polymerization mixture (Fig. 17), and studied their influence on the morphology and electrical conductivity of the prepared polymer.

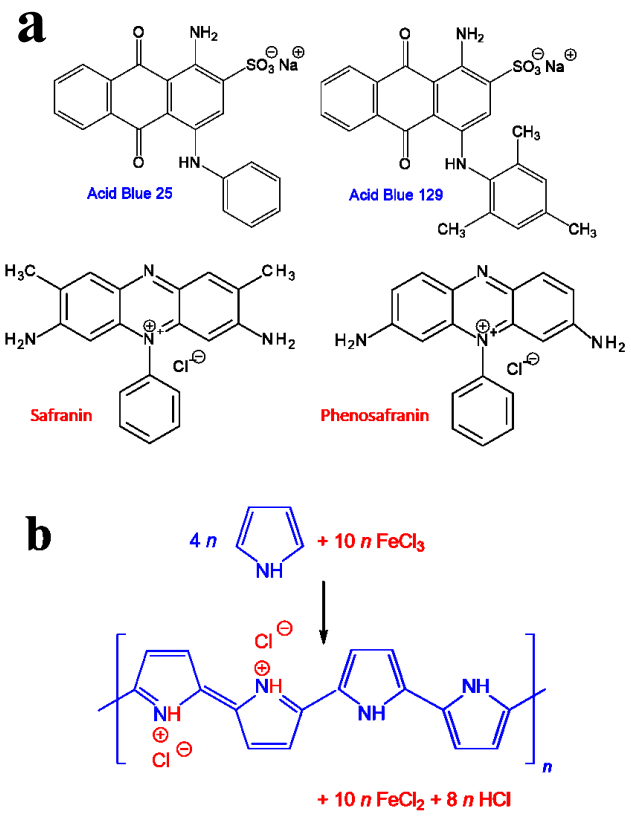

Figure 17. Chemical formulae of dyes (a) and scheme of pyrrole polymerization (b).

Effect of anionic dyes

The addition of two closely related anionic dyes to the polymerization mixture, despite the similarity in their molecular structure (Fig. 17 a), resulted in different PPy morphologies **[Attachment 3]**. In the presence of Acid Blue 25, PPy nanowires were formed, while in the presence of Acid Blue 129 globular morphology was preserved (Fig. 18).

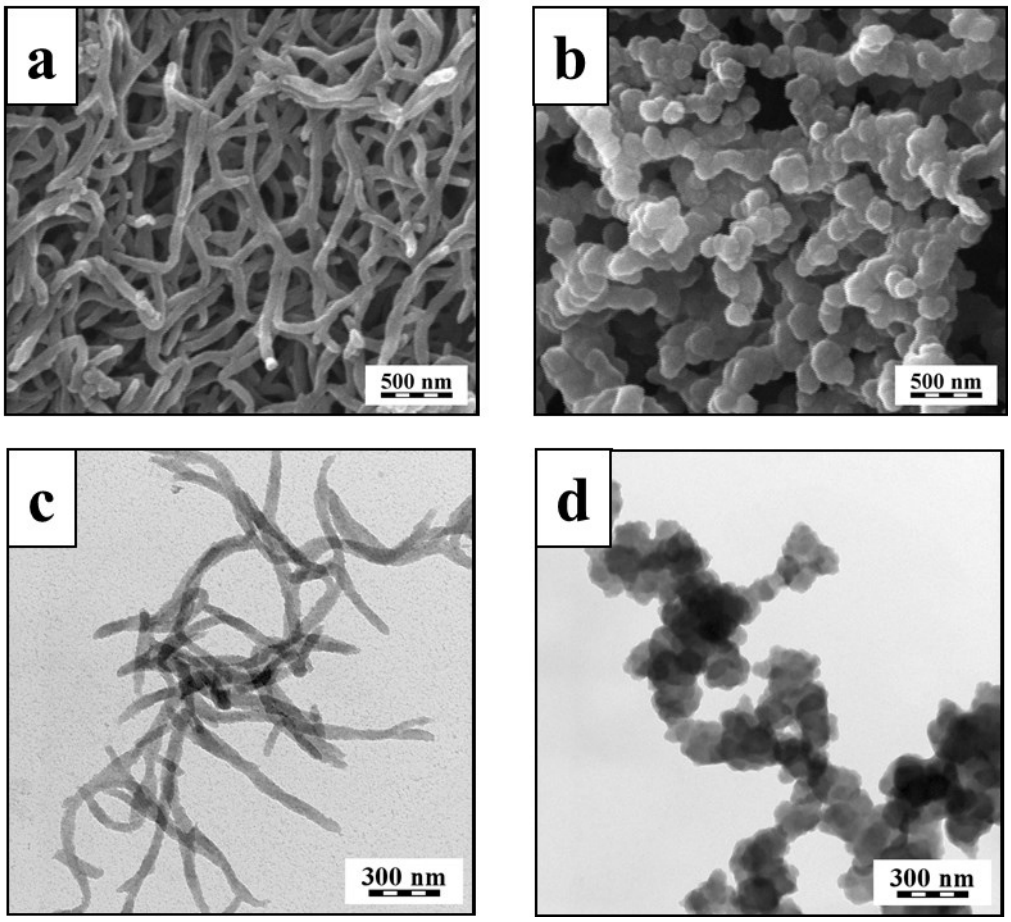

Figure 18. SEM (a, b) and TEM (c, d) micrographs of PPy prepared in the presence of Acid Blue 25 (a,c) and Acid Blue 129 (b, d). **[Attachment 2]**

Table 2. Series 1: Effects of pyrrole concentration on the conductivity and on the polymerization yield for the PPy prepared in the presence of Acid Blue 25 and 129 (*Series 1)*. [Dye]/[Pyrrole]=0.05, [Oxidant]/[Pyrrole]=1.

[Py] (M)	**Conductivity (S cm^{-1})**		**Yield (g g^{-1} pyrrole)**	
	AB 25	**AB 129**	**AB 25**	**AB 129**
0.05	20 ± 0.3	18 ± 0.2	0.71	0.16
0.1	43 ± 0.6	31 ± 0.5	0.72	0.32
0.15	45 ± 0.4	38 ± 0.6	0.73	0.50
0.2	52 ± 0.4	40 ± 0.2	0.76	0.67

In both cases, however, the presence of the dye affected the electrical conductivity. Two series of experiments were performed. In the first one we changed the concentration of PPy and other components in the reaction mixture keeping their mutual ratio constant

(Table 2). In this series, the conductivity increased with increasing pyrrole concentration from 20 S cm^{-1} to 52 S cm^{-1} in the case of Acid Blue 25, and from 18 S cm^{-1} to 40 S cm^{-1} in the case of Acid Blue 129.

In the second series, the concentration of pyrrole and dye was fixed but the oxidant concentration varied (Table 3). When the oxidant-to-pyrrole mole ratio increased from 1.5 to 3, the conductivity of PPy nanowires further increased up to 62 S cm^{-1}. The conductivity of globular PPy prepared in the presence of Acid Blue 129, was slightly lower than in the previous case, but still much higher than the polymer prepared without the dye. The obtained results suggest that the conductivity is not always dependent of the morphology, but rather on the degree of polymer chain ordering.

Table 3*:* Effects of oxidant-to-pyrrole mole ratio on the conductivity and the yield of PPy prepared at various oxidant-to-pyrrole mole ratios (*Series 2)*. [Pyrrole]=0.2 M, [Dye]=0.01 M.

[Ox]/[Py]	**Conductivity (S cm^{-1})**		**Yield (g g^{-1} pyrrole)**	
	AB 25	**AB 129**	**AB 25**	**AB 129**
1.5	45 ± 0.3	39 ± 0.4	1.10	0.95
2	55 ± 0.3	36 ± 0.5	1.41	1.20
2.5	60 ± 0.5	35 ± 0.2	1.53	1.40
3	62 ± 0.7	40 ± 0.4	1.55	1.43

Effect of cationic dyes

Safranin and phenosafranin were chosen to study the effect of cationic dyes in the polymerization mixture on the properties of PPy. We found that these dyes have also an impact on the polymer morphology, namely, they support the one-dimensional growth of PPy **[Attachment 4]**. The TEM analysis revealed a mixture of nanofibers and nanotubes in the polymer when prepared with the addition of safranin (Fig. 19 a), while in the case of phenosafranin, much thicker nanotubes accompanied by globular particles were formed (Fig. 19 b). The influence of dye concentration as well as of the oxidant-to-monomer molar ratio on the conductivity of PPy was investigated in details.

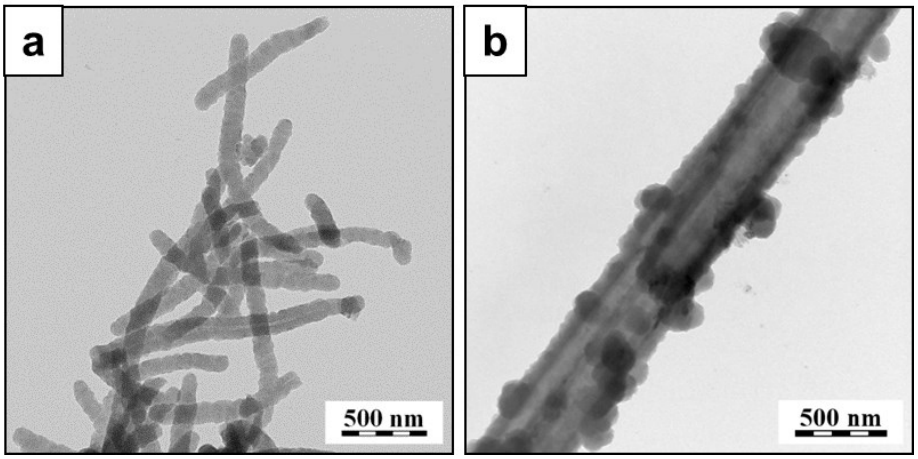

Figure 19. TEM micrographs of polypyrrole prepared in the presence of (a) safranin and (b) phenosafranine.

Similar to the case of anionic dyes, the addition of cationic dyes had a significant effect on increasing the conductivity of PPy. The highest conductivity of 35 S cm $^{-1}$ and 10.5 S cm $^{-1}$ was obtained with 4 mM of safranin and 2 mM of phenosafranine, respectively (Fig. 20 a). This increase in conductivity can be explained by better PPy chain organization in one-dimensional structures than in globules, and more favorable dopant distribution along polymer chains. Based on the highest conductivity of PPy prepared with 4 mM safranin concentration, it was chosen for further optimization of the polymerization by finding the most suitable oxidant-to-pyrrole mole ratio. It was found that stochiometric ratio of 2.5 used for the preparation of the globular PPy is also the best for the synthesis of one-dimensional structures and gives the highest conductivity (Fig. 20 b). Moreover, the good stability of conductivity of one-dimensional PPy was clearly demonstrated, reaching extremely high oxidant-to pyrrole mole ratio of 15 with no signs of overoxidation or degradation of PPy.

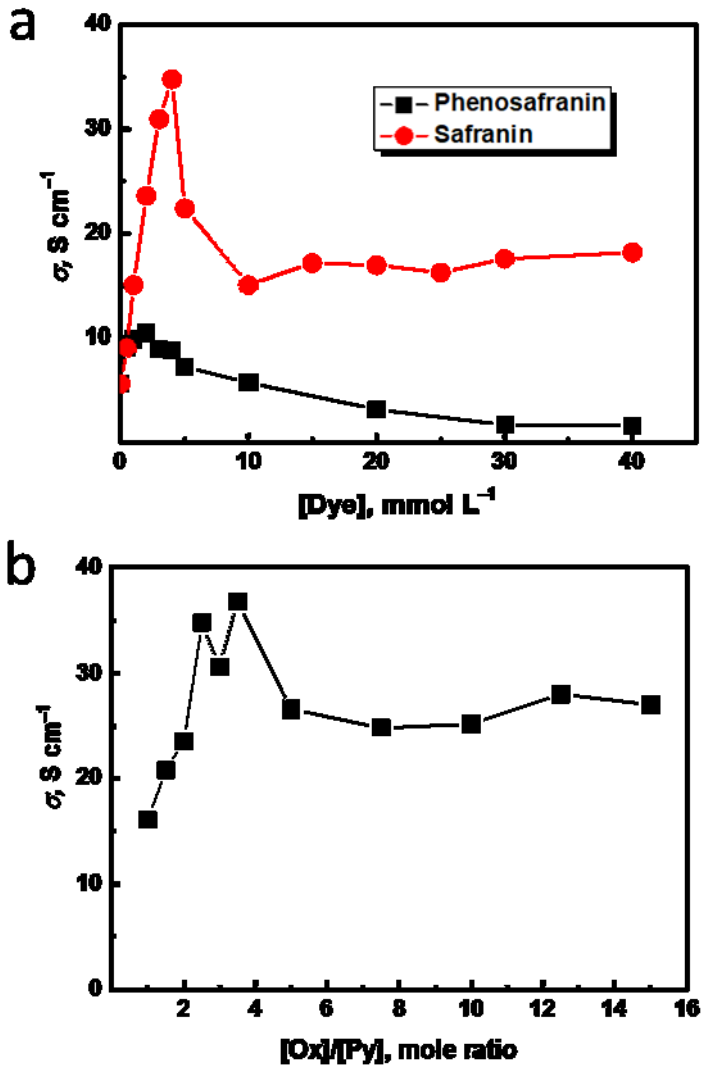

Figure 20. The dependence of conductivity on (a) the molar concentration of safranin or phenosafranin used in the synthesis and (b) iron(III) chloride to pyrrole mole ratio, [Ox]/[Py] where 4 mM of safranin was used.

It is well known that the polymerization temperature also plays a key role in obtaining polymers with high conductivity. For example, it was shown that polyaniline prepared at -24 °C possess higher molecular weight and conductivity, compared to that prepared at room temperature [122]. Based on this finding we studied the effect of the polymerization temperature (from -80 to 50 °C) on the electrical conductivity and charge transport mechanism in PPy prepared in the presence of 4 mM safranine at 2.5 oxidant-to pyrrole mole ratio **[Attachment 4]**. The polymerization temperature had a crucial impact on the morphology of PPy prepared in the presence of safranin; at 50 °C the mixture of globules and fibrillar particles was found, at room temperature well-defined fibers were produced, while temperature decreased down to -24 °C led to interconnected fibers with much smaller dimensions. Further decrease of temperature produced a mixture of irregular flakes and nanotubes **[Attachment 4]**.

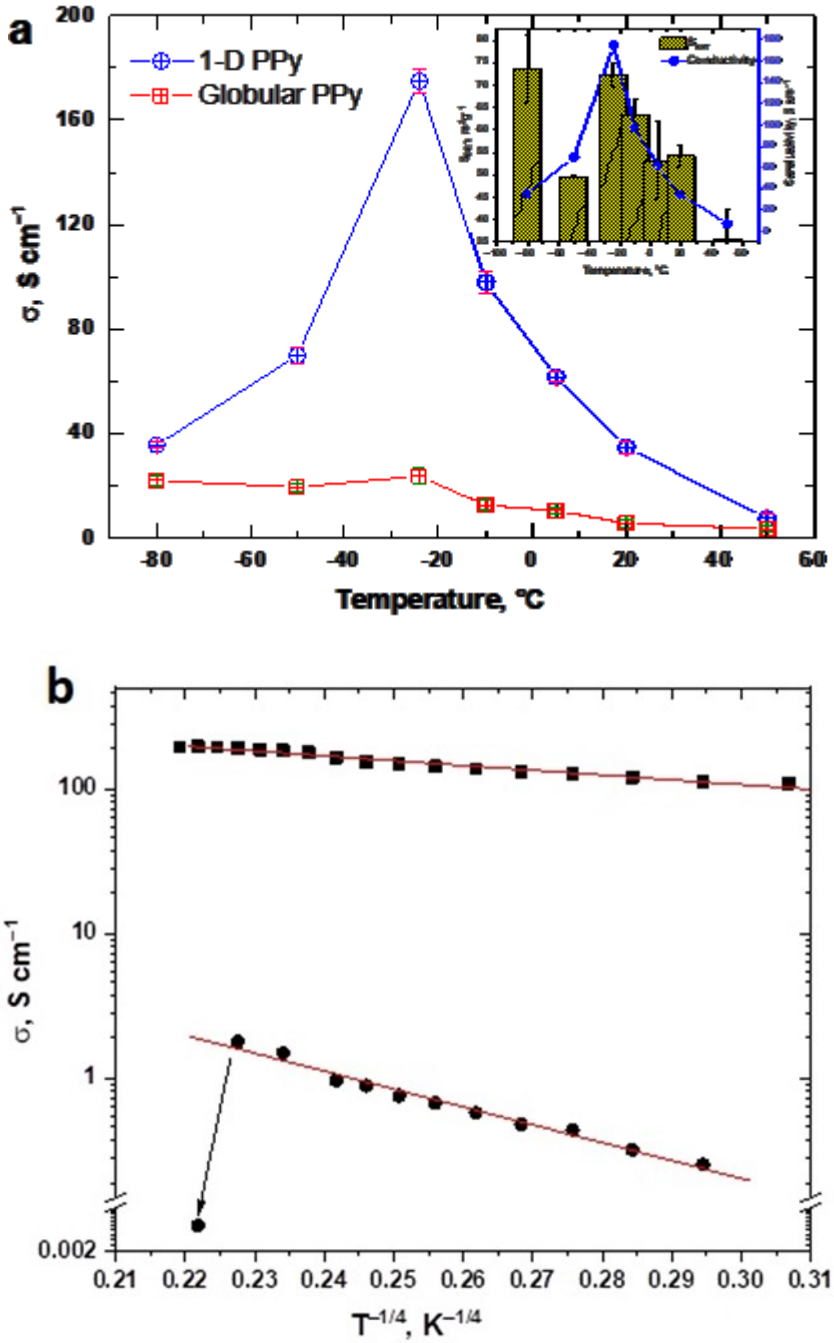

Figure 21. (a) The influence of the polymerization temperature on the conductivity of the one-dimensional PPy prepared in the presence of safranin, and of the globular PPy (inset shows the correlation between conductivity and specific surface area of one-dimensional PPy). (b) Temperature dependence of the conductivity of one-dimensional PPy prepared at −24°C (full squares) and globular PPy (full circles) plotted as a function of $T^{-1/4}$.

The polymerization temperature was also found to have a marked effect on the electrical conductivity of one-dimensional PPy, but having less effect on conductivity of the globular PPy (Fig. 21 a). At high polymerization temperature reaching 50 °C both PPys have

similar conductivity, independently if prepared in the presence or absence of safranin, but with decreasing polymerization temperature the difference between two structures was clearly visible. When the polymerization proceeded at -24 °C the maximum value of conductivity reached 175 S cm^{-1} in the case of one-dimensional PPy, which is the highest value reported in the literature for PPy powder. This increase is attributed to a higher level of protonation, confirmed by Raman spectroscopy, and to a much better rearrangement of polymer chains in the thinner fibers. The conductivity of globular PPy also increased, but reached only 23 S cm^{-1}. A further decrease of the polymerization temperature led to a decrease in conductivity for both types of PPy.

In order to better understand the nature of charge carrier transport in such highly conducting one-dimensional PPy, the temperature dependence of conductivity was measured in a wide range of temperatures from -140 to +160 °C. As it is shown on Fig. 21 b, in the interval from −160 to 140 °C PPy shows a typical semiconductor behaviour with a positive slope. After exceeding 140 °C a slight decrease of conductivity was observed, which can be attributed to the deprotonation of the PPy. This drop of conductivity is much smaller for 1-D PPy than for the globular one, which means that the dopant molecules are much better anchored in one-dimensional PPy structure. The conductivity *vs* $(T_0/T)^{1/n}$ plot was fitted for various values of n using the least square method and $n = 4$ was found as the best fit of the experimental data. It clearly points to the 3-D variable range hopping as a charge transport mechanism. The T_0 value obtained from the temperature dependences of the conductivity of one-dimensional PPy was smaller compared to that for globular one. It confirms a longer delocalization of carriers and higher level of doping in the molecularly well-ordered domains of PPy prepared in the presence of safranin. In addition, the frequency independent AC conductivity supports the idea that the charge transport proceeds through homogeneous and rather compact grains.

3.1.3 Polyaniline thin films

Colloidal conducting polymers, like PANI and PPy, seem to be suitable materials for the fabrication of semiconducting layers using various printing and additive manufacturing technologies. Series of polyaniline colloidal dispersion in water stabilized with various amount of poly(*N*-vinylpyrrolidone) (PVP) and doped with hydrochloric or phytic acid (PA) were prepared and used as conducting inks for the preparation of transparent (Fig. 22) thin films by a spiral bar technique (Fig 22 a) **[Attachment 7]**. The formation of protonated PANI salt in all these colloids was confirmed by UV-vis and Raman spectroscopy. PANI colloids have spherical morphology with mean particle size ~300 nm or ~360 nm, when doped with HCl or PA, respectively.

The SEM images revealed that globular morphology of particles was preserved after casting the films, however the films with higher PVP concentration and doped with PA possessed much smoother surface then PANI films doped with HCl. This was also confirmed by AFM, where average surface roughness value decreased from 64 to 27 nm (Table 4).

Table 4. Thickness, conductivity, contact angle and roughness of PANI films. **[Attachment 7]**

PVP concentration, (wt%)	**Thickness, (μm)**	**Conductivity, (S cm^{-1})**	**Contact angle, (degree)**	**Roughness (R_a), (nm)**
PANI-PA-PVP				
1	2.8	7×10^{-5}	102	92
2	0.8	4×10^{-5}	99	81
3	1.1	9×10^{-6}	85	52
4	2.2	5.9×10^{-6}	71	17
PANI-HCl-PVP				
1	1.3	5×10^{-3}	10	64
2	1.7	1×10^{-3}	15	60
3	1.5	1×10^{-5}	26	33
4	1.5	4×10^{-6}	38	27

The highest conductivity values 7×10^{-5} S cm^{-1} and 5×10^{-3} S cm^{-1} were found for PANI films doped with PA and HCl, respectively, where 1 wt% of PVP was used (Table 4). As expected, the conductivity of films decreased with increasing concentration of PVP due to increased content of non-conducting fraction. The conductivity was similar to that reported in literature for spray coated PANI colloids stabilized with PVP [123], but it was slightly lower than for films grown on substrates immersed in the reaction mixture during polymerization [124]. The concentration of PVP as well as the dopant type was found to markedly influence the wettability of the films. The PANI films doped with PA and containing 1 wt% of PVP showed hydrophobic properties with the contact angle 102°, while the films containing the same PVP concentration but doped with HCl had hydrophilic properties, showing the contact angle 10° (Table 4).

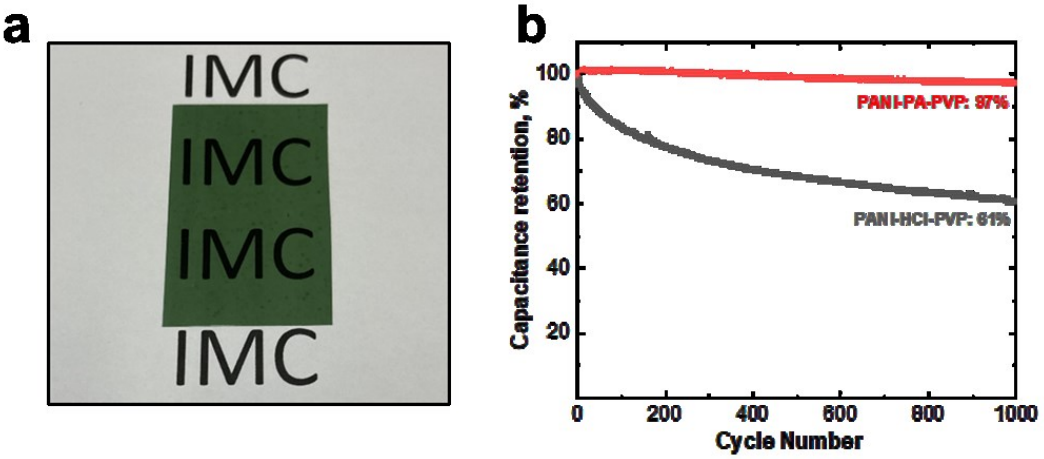

Figure 22. The photograph of the PANI film cast on a glass substrate (a), and electrochemical cycling stability of PANI-HCl-PVP and PANI-PA-PVP dispersions (1 wt% PVP) during 1000 subsequent cycles (b). **[Attachment 7]**

Electrochemical properties of drop cast PANI dispersion were studied by cyclic voltammetry. The film doped with HCl showed higher electrochemical activity, which is contributed to its higher conductivity (Table 4). Although the initial electroactivity of the films doped with PA was lower, their stability was found to be better (Fig. 22 b). The PANI-PA films retained 97% of its initial capacitance after 1000 cycles while, in the case of PANI-HCl films, only 61% was observed. The combination of high capacitance retention together with hydrophobicity, easy scalability, and possibility of using low-cost deposition techniques, make PANI colloidal dispersions doped with PA a promising material for further applications in printed electronics.

3.2 Impedance studies of conducting polymer-clay composites

A series of poly(*p*-phenylenediamine)/montmorillonite (PPDA/MMT) composites (Fig. 23) with various monomer to clay ratios was prepared by in situ chemical oxidation of monomers within the MMT gallery in order to investigate the conduction mechanism at different temperature regions **[Attachment 6]**. The successful intercalation process was confirmed by XRD measurement. The final amount of PPDA in the composites was calculated based on TGA results. As the FTIR and Raman spectroscopies showed, the polymer or oligomers were obtained, depending on the monomer to MMT ratio in the reaction mixture. No globular particles of neat PPDA were seen, all PPDA was embedded within the MMT gallery and/or as a thin film covering the MMT surface. The highest observed DC conductivity of the composites was found to be close to the value of the neat MMT of ~10^{6} S/cm; significantly higher than the DC conductivity of pristine PPDA (Table 5).

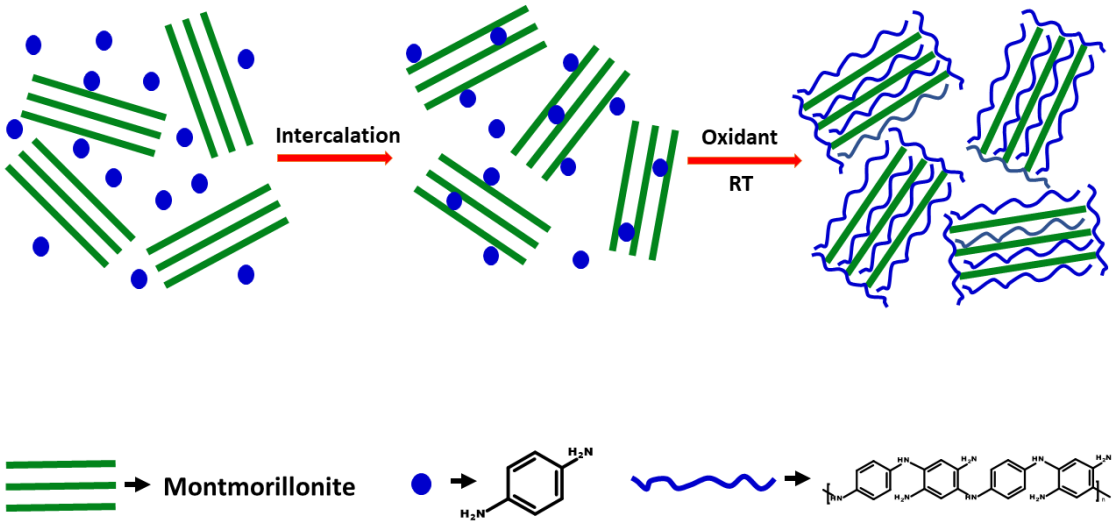

Figure 23. Preparation scheme of PPDA/MMT composites.

Table 5. The montmorillonite and PPDA content, DC conductivity and activation energy of PPDA/MMT composites.

Sample code	MMT content in composites, (wt%)	DC conductivity, σ (S cm^{-1})	Activation energy, E_a (eV)		
			evaluated from relaxation time vs. 1/T	evaluated from DC conductivity vs. 1/T	
				High temperature region	Low temperature region
PPDA	0	7.2×10^{-11}	0.57	0.64	0.02
PPDA-2	81	3.4×10^{-11}	-	-	-
PPDA-5	82	1.6×10^{-11}	0.69	0.58	0.05
PPDA-10	92	2.5×10^{-8}	-	-	-
PPDA-15	92	3.4×10^{-8}	-	-	-
PPDA-25	93	2.2×10^{-7}	-	-	-
PPDA-35	94	1.0×10^{-6}	0.44	0.34	0.06
PPDA-50	93	9.2×10^{-7}	0.54	0.42	0.12

For deeper understanding the conduction mechanism in these composites, a comprehensive impedance characterization has been performed, where impedance was measured in a broad frequency (10^{-2} Hz to 10^{7} Hz) and temperature range (113 K ≤ T ≤ 433 K). In these composites, conductivity arises from both electronic and ionic contributions. From the shape of ε′ vs f curve at low frequencies an electrode polarization is seen causing an increase of the dielectric constant (Fig. 24). The value of ε′ was found to be smaller in the composites with lesser content of MMT. It can be explained by smaller contribution of water molecules captured in MMT, which increase the dielectric constant by their dipolar contribution. The shape of the frequency dependence of ε′′ in the low frequency region, with the slope around –1, points to the ion transport whereas the slope > –1 is a proof of electrode polarization (Fig. 25). Increased temperature causes the ions to dissociate, resulting in an increase in the dielectric polarization. Since this dissociation of ions is limited at low temperature, only polarons remain to be major charge carriers, which is reflected in low permittivity.

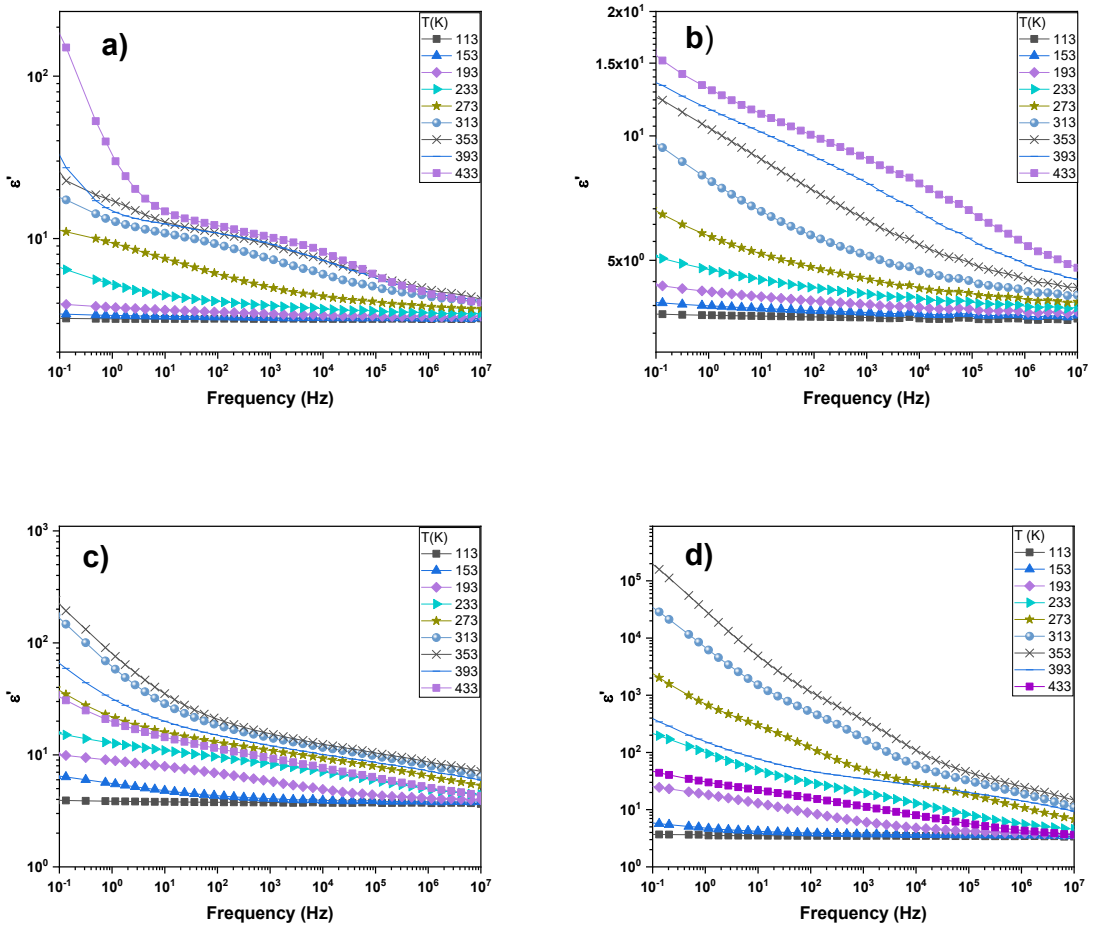

Figure 24. Frequency dependence of real part of permittivity at different temperatures for (a) pure PPDA and PPDA/MMT composites (b) PPDA-5, (c) PPDA-35 and (d) PPDA-50.

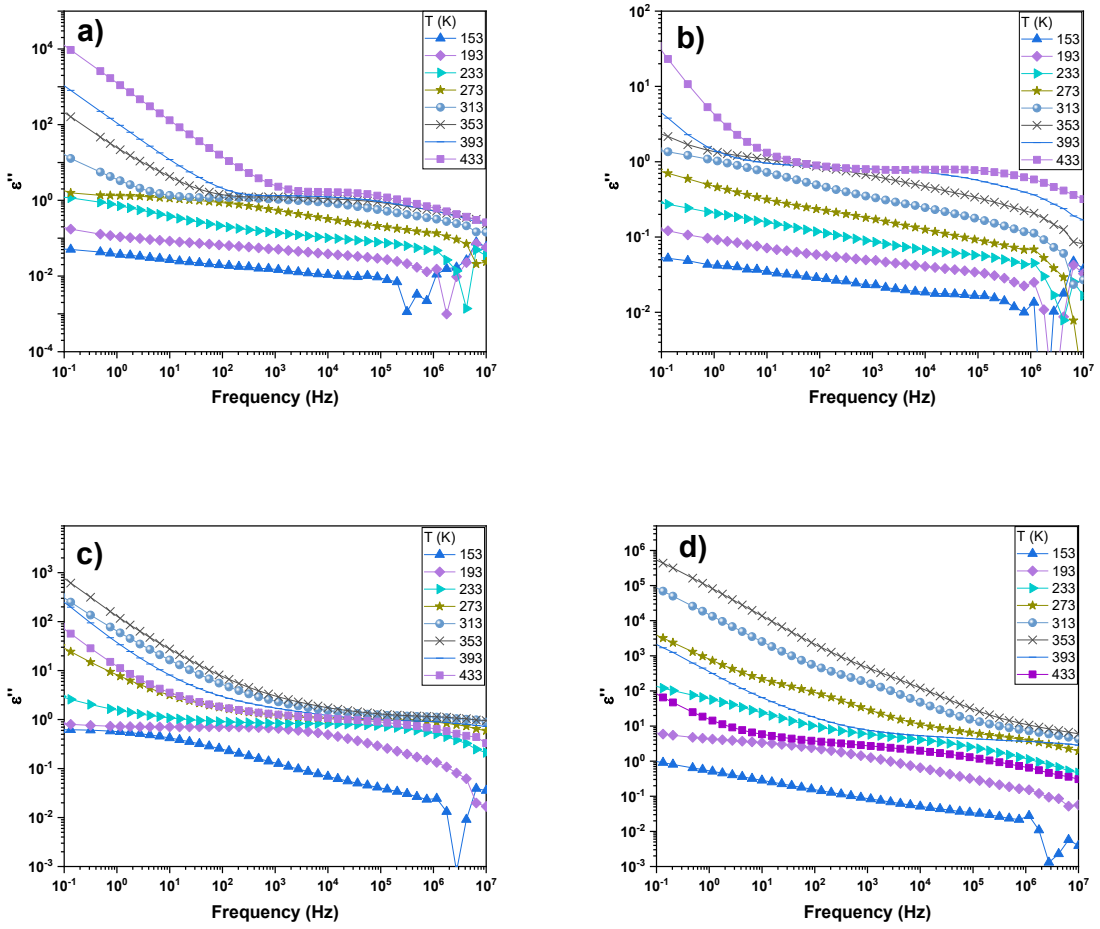

Figure 25. Frequency dependence of imaginary part of permittivity at different temperatures for (a) pure PPDA and PPDA/MMT composites (b) PPDA-5, (c) PPDA-35 and (d) PPDA-50.

From the maxima in the spectra of M'' at different temperatures the values of relaxation time were calculated and plotted as a function of temperature as shown in Fig. 26. The curves follow the Arrhenius law from which the calculated activation energy is presented in the Table 5. Fig. 27 shows frequency dependences of real part of conductivity σ'at different temperatures. Using Jonscher's law (Eq. 21), σ_{dc}, and parameters A and s were calculated. It was found that PPDA-35 AND PPDA-50 had higher conductivity compared to the pristine polymer. This can be explained by highly ordered polymer chains in the gaps between MMT layers, forming a compact structure preferential for the efficient charge transport.

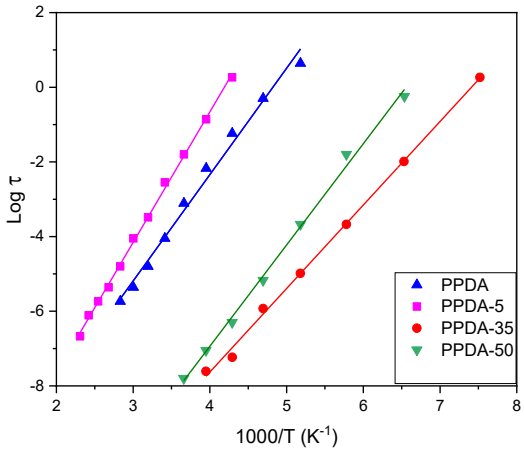

Figure 26. Plot of relaxation time vs reciprocal temperature for PPDA and PPDA/MMT composites.

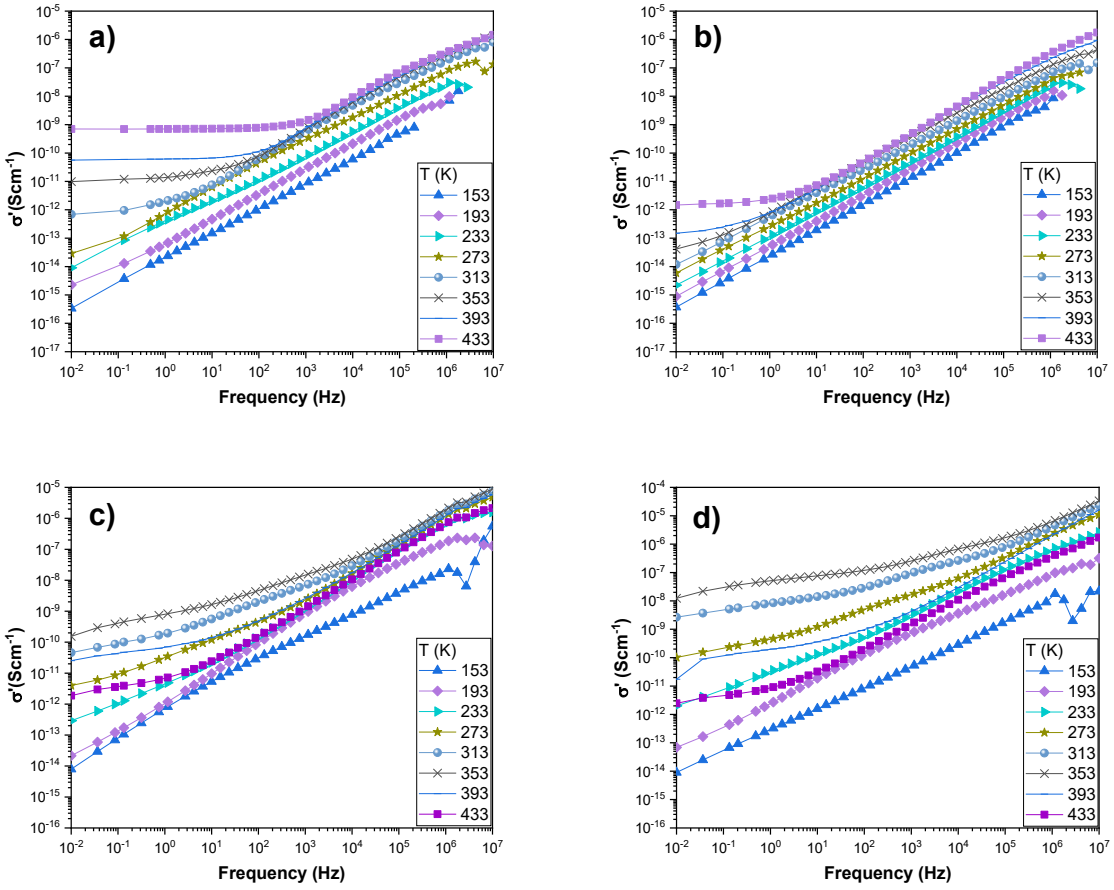

Figure 27. Frequency spectrum of real part of AC conductivity at different temperatures for (a) PPDA and PPDA/MMT composites (b) PPDA-5, (c) PPDA-35 and (d) PPDA-50.

From the temperature dependence of the DC conductivity, σ_{dc}, the activation energy was calculated (Table 5). The fitting was done separately in two temperature regions as shown in Fig.28. It can be clearly seen that there are two activation energies, different in the high and low temperature regions. At higher temperatures, ion dissociation takes place and, hence, ionic conductivity increases with increasing temperature, whereas ions lack enough energy to move to neighbouring sites and remain caged at low temperature (Fig. 28). In this low temperature region polarons are the prevailing mobile charge carriers. The break in the slope for sample PPDA-35 and PPDA-50 occurred at about 200 K, which signifies the motion of water-polymer complex in the amorphous region. The decrease in conductivity above 353 K is associated with the evaporation of intercalated water. For remaining samples, the change in slope occurred at 273 K, which can be attributed to a phase transition associated with local structure.

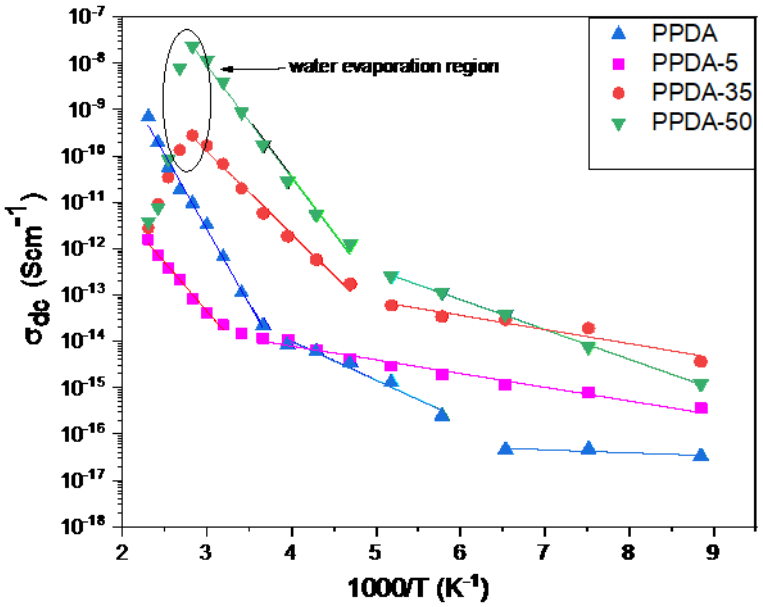

Figure 28. Variation of DC conductivity with reciprocal temperature. The solid lines represent fitting according to Equation (2).

As shown in Fig. 29, the value of s decreases with increasing temperature for all PPDA/MMT composites under study. This can be expected since charge carriers have to hop between sites over the potential barrier, showing correlated barrier hopping of polarons at lower temperature. It can be noted from the values of W_M that the polarons are the major charge carriers, because for bipolaronic transport mechanism, four times higher W_M would be required [125].

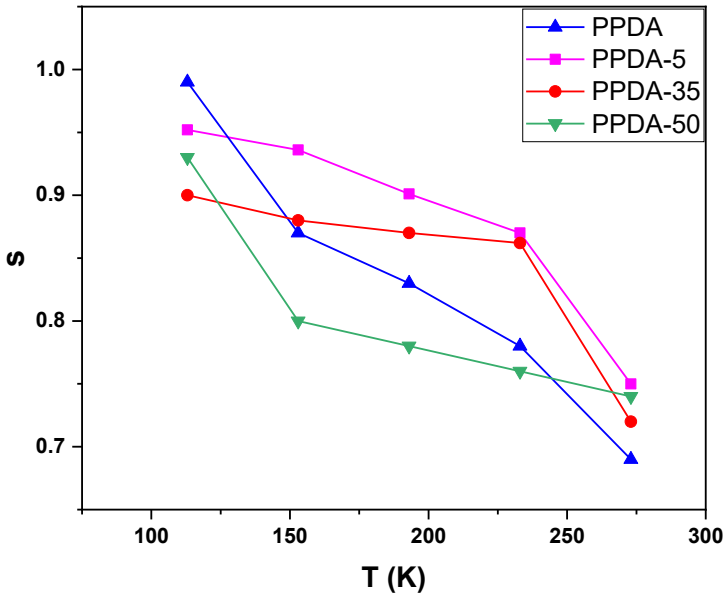

Figure 29. Variation of exponent parameter s with temperature for PPDA and PPDA/MMT composites. The solid lines are drawn for clarity.

3.3 Electrochromic properties of iron(II) metallo-supramolecular polymers

Four Fe(II) metallo-supramolecular polymers were prepared with unimers based on thieno[3,2-b]thiophene central unit and various linkers (none, ethynediyl, 1,4-phenylene, and 2,2′-bithophene-5,5′-diyl) end-caped with bis(2,2′:6′,2″-terpyridin-4′-yl end-groups, denoted as Fe-Tt, Fe-TtE, Fe-TtPh and Fe-TtB (Fig. 30). The electrochromic properties of spin coated films of these MSPs polymers were investigated by spectroelectrochemical measurements and atomic force microscopy. Finally, their electrochromic properties were tested in a functional device [**Attachment 5**].

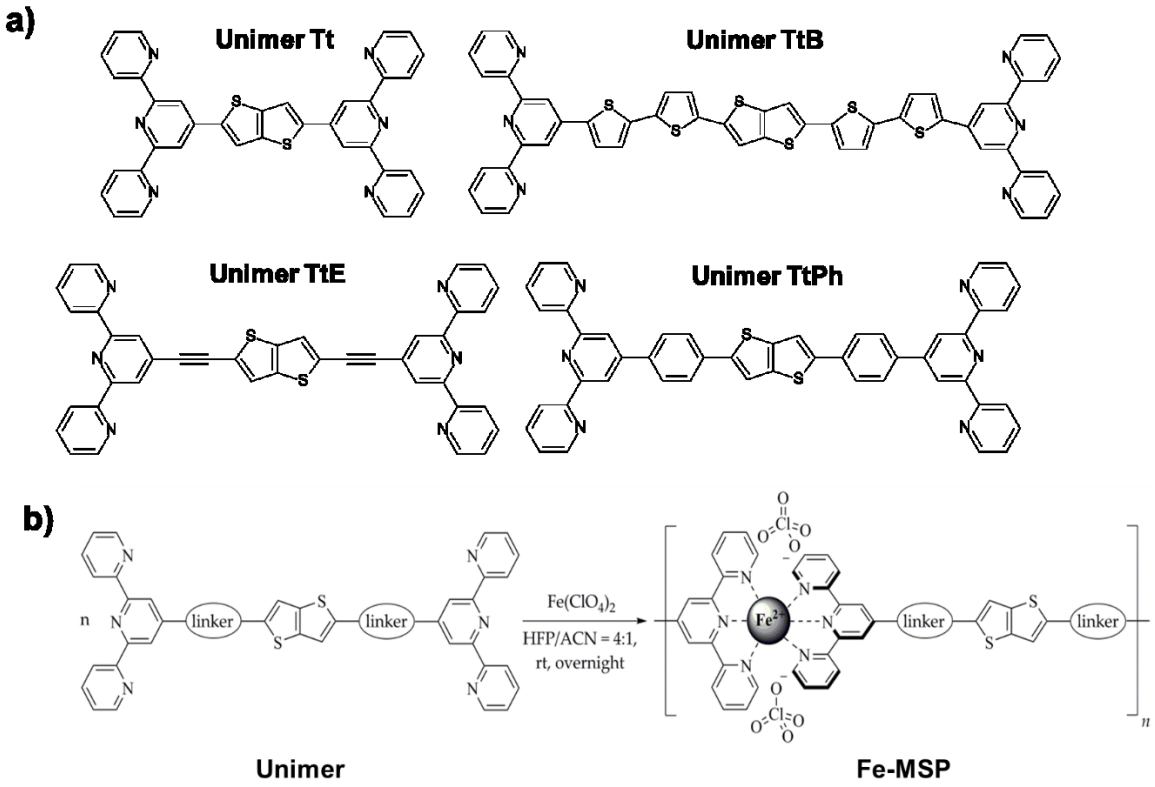

Figure 30. Prepared unimers (a) and their self-assembly to Fe^{2+}-MSPs (b).

For understanding the redox behavior of Fe-MSPs films, cyclic voltammetry was carried out in oxygen-free acetonitrile solution containing 0.1 M tetrabutylammonium hexafluorophosphate with the scan rate variation from 20 to 1000 mV/s (Fig. 31). All the films show one reversible redox wave corresponding to the Fe^{2+} to Fe^{3+} oxidation, which is in a good agreement with similar systems reported in literature [126]. The peak separation increases with the scan rate, which indicates a quasi-reversible redox reaction, similarly, as observed by other authors in metallo-supramolecular coordination polymers [127]. The peak current density (inset of Fig. 31) was found to be linearly proportional to the square root of the scan rate, indicating diffusion control redox process in all the Fe-MSPs regardless of the linker type. With increasing the linker size, the volume fraction of unimer units increases lowering thus the Fe ion concentration which, results in a smaller proportionality constant.

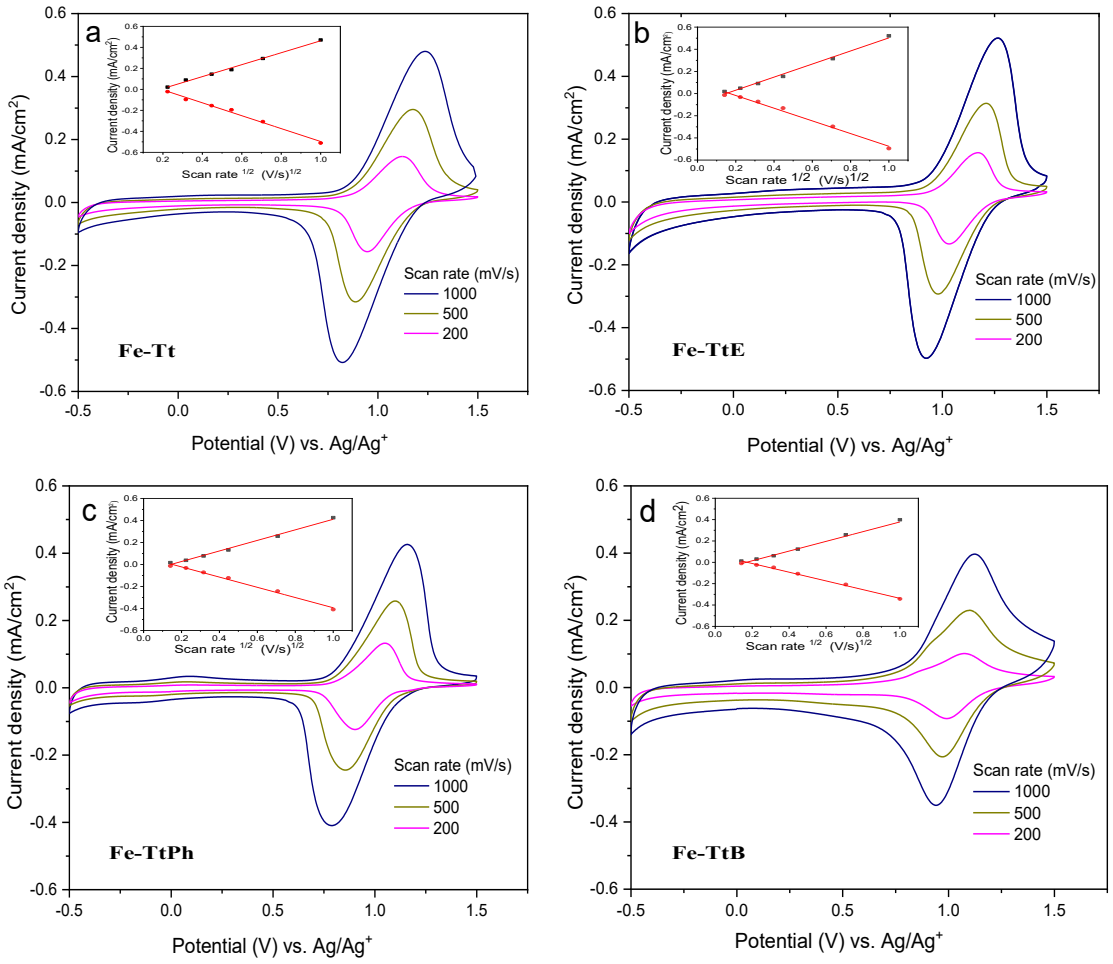

Figure 31. Cyclic voltammograms of Fe-MSP films under different scan rates. Insets represents the dependences of the anodic and cathodic peak currents on the square root of the scanning rate. [**Attachment 5**]

The UV/vis/NIR absorbance spectra of all Fe-MSPs shown in Fig. 32 possess two distinct absorption peaks in their neutral state: i) the peak centered around 600 nm assigned to the MLCT transition and ii) the shorter wavelength peak centered around 450 nm assigned to the π-π^* transition in unimer. The spectra clearly manifest that MLCT band disappears in all the samples after the electrochemical oxidation of Fe(II) to Fe(III) and the unimer band is redshifted. Fe-TtB MSP showed reversible intense NIR absorption peak opening the gateway for NIR electrochromic devices.

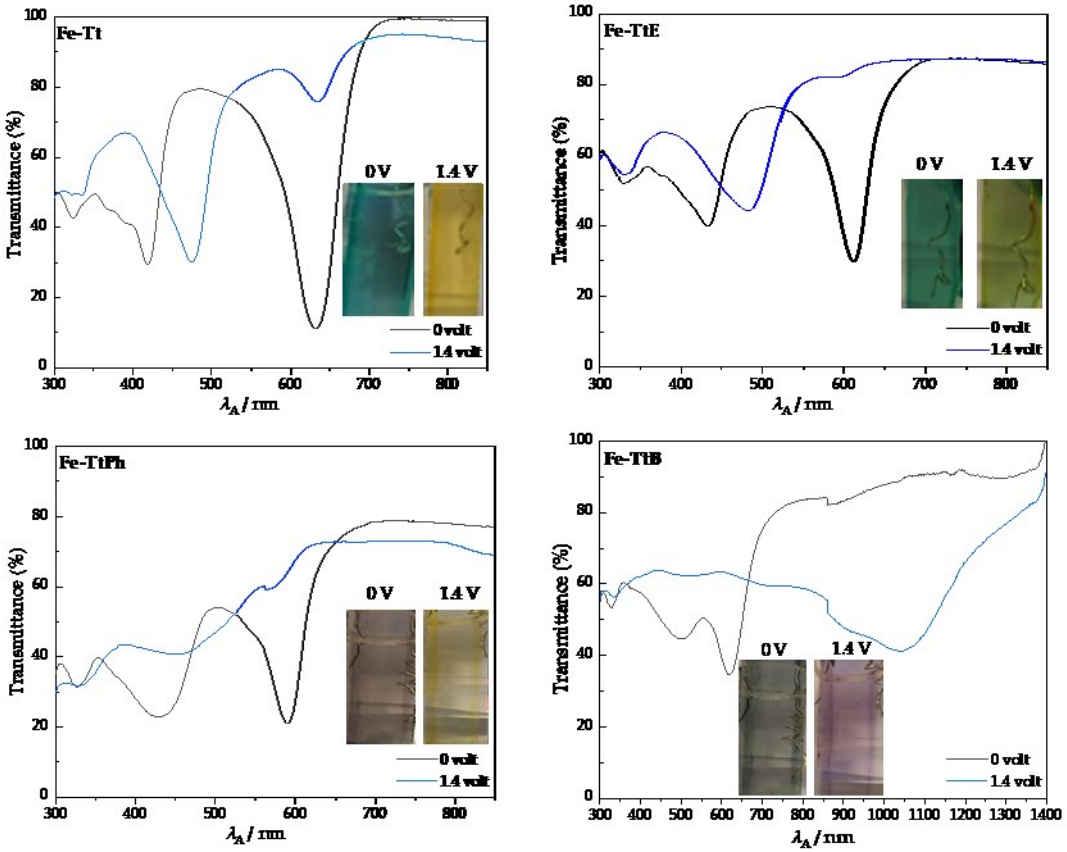

Figure 32. UV/vis/NIR absorption spectra of Fe-MSP films in the colored (black curve, 0 V) and bleached (blue curve, 1.4 V) state. Insets: The photographs of Fe-MSPs films in colored and bleached states. [**Attachment 5**]

Different parameters, like coloration efficiency (CE), optical density (ΔOD), switching time, cycling stability, are uniquely important according to the targeted potential application of ECD. Here, we report on standard parameters to quantify the ECD properties, which are summarized in Table 6.

Since ΔOD does not vary linearly with the charge Q during the complete electrochromic process, usually the total charge is reported, required to attain 95% of total change in color. This limit seems reasonable since remaining 5% is barely visible (Fig. 33). For the Fe-Tt film the highest coloration efficiency of 641 $cm^2\ C^{-1}$ was found, which is quite competitive value among those reported in literature [128,129]. It should be noted that only the faradaic current controls the redox activity, hence net current based calculation can mislead the CE values. For this reason, a tandem charge ingress/egress was used to calculate Q values by the instrument for chrono-coulometric measurement [130] as described in the experimental section 2.3.

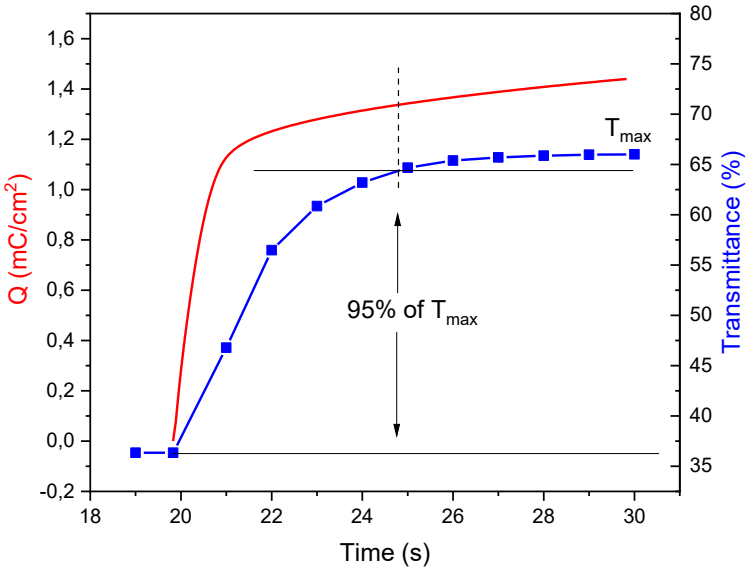

Figure 33. Simultaneous time-evolution of %T (blue curve) and charge density (red curve). The level of 95% of the full optical transmittance change is taken to calculate the coloration efficiency. [**Attachment 5**]

The optical contrast of Fe-MSPs films was tested under the repeated step change of potential between 0 and 1.4 V. The highest optical contrast (Table 6) measured for MLCT band was found to be 64.5% for Fe-Tt film whereas Fe-TtB showed the lowest value of about 29%. This value is comparable to those found in literature for similar systems. For example, Zhu et al. reported the optical contrast around 20%. The film Fe-TtB also showed comprehensive optical contrast at 1041 nm, which eventually disappeared after few repetition cycles.

Table 6. Electrochromic performance of Fe-MSPs films: λ_{MLCT} - the wavelength of the MLCT band, ΔT – optical contrast, ΔOD – change in optical density, t_b - bleaching time (neutral to oxidized state), t_c - coloring time (oxidized to neutral state), CE – coloration efficiency.

MSP	λ_{MLCT} (nm)	ΔT (%)	ΔOD	t_b (s)	t_c (s)	CE ($cm^2\ C^{-1}$)
Fe-Tt	632	64.5	0.82	1.1	1.8	641
Fe-TtE	612	54.5	0.42	3.7	1.8	229
Fe-TtPh	590	43.0	0.44	1.8	1.8	332
Fe-TtB	618	29.0	0.25	4.6	1.7	173

The coloring time (t_c), which is connected to the reduction process, was found to be

about 1.8 s, nearly the same for all the samples (Table 6). However, the bleaching time (t_b) corresponding to the oxidation process was found to differ significantly for various SMPs. This can be attributed to the different diffusion rate of counter-ions into the bulk of the polymer films during the oxidation process and ion/charge transport between the electrolyte and the film. Additionally, the coloring time was also found to be dependent on the concentration of the redox species. During reduction, it is much easier for the counter ions to diffuse out of the partly swollen film.

Since the material Fe-Tt had the best electrochromic properties, it was used to construct an ECD operating in transmission mode (Fig. 34 a). The device consisted of two transparent conducting electrodes (ITO), where one was coated with EC material, and a gel electrolyte sandwiched between these electrodes as shown schematically in Fig. 34 b. The gel electrolyte used in our ECD was prepared by mixing poly(methyl methacrylate) (3.5 g), propylene carbonate (10 mL), and $LiClO_4$ (1.5 g) as suggested by Higuchi et al. [103]. Its ionic conductivity was 2.3×10^{-3} S cm^{-1}, obtained as a low frequency limit of the real part of complex conductivity measured using broadband impedance spectroscopy. The main benefits of the device that employs this gel electrolyte are its good chemical and thermal stability, durability and cyclability. In liquid electrolyte the films usually delaminate from the substrate by partial film dissolution during repetitive cycling, which is not the case in the device with the gel electrolyte. The optical contrast of the prepared ECD was 59.6 % at 637 nm wavelength, and the ECD showed high stability during repeated cycling (Fig. 34).

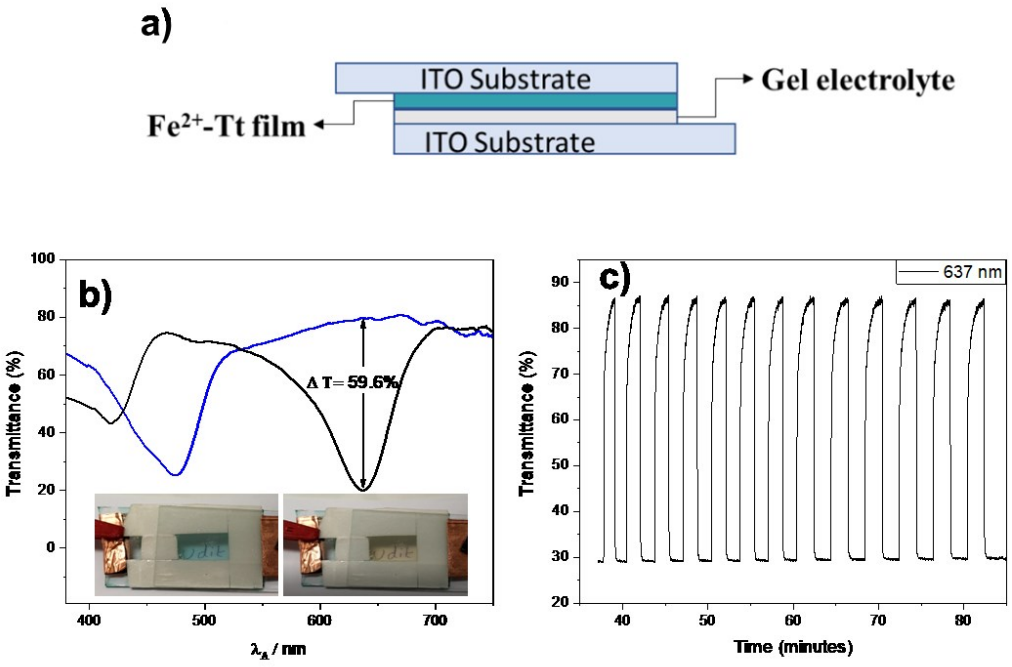

Figure 34. Schematic representation of ECD (a), UV/vis diffusion transmittance spectra of Fe-MSP ECD in the colored (black curve, 0 V) and bleached (blue curve, 1.4 V) state (insets show the photographs of ECD in colored and bleached state) and optical response of ECD device at indicated wavelength to the periodic cycling (c). **[Attachment 5]**

4. Conclusions

The presented experimental study performed on two conducting polymers, PANI and PPY, and their composites shows that the electrical properties can be markedly influenced by optimization of the polymer morphology. Influenced by intermolecular interactions with the surface of inorganic fillers or with various organic dyes present in the reaction mixture during polymerization the polymer can acquire globular, nanofibrillar or nanotubular form with the direct impact on the mechanism of the charge carrier transport. The morphology and electronic properties can be also modified by using oligomers with shorter conjugated sequences linked together in metallo-supramolecular coordination polymers. It was documented by several experimental observations:

- Conductivity studies of PPy/MoS_2 composites showed that DC conductivity was significantly improved in the case of composites (5–13 S cm^{-1}) compared to that of neat components (PPy 1 S cm^{-1}; MoS_2 10^{-6} S cm^{-1}). Improved conductivity of the composites occurred due to better PPy chain ordering, efficient for the transport of charge carriers, during the growth of thin PPy film on MoS_2 surface. The variable-range hopping was found to be the main charge transport mechanism.
- The addition of organic dyes (anionic or cationic) to the polymerization of pyrrole was found to have direct impact on converting the PPy morphology from globular to nanofibrillar and nanotubular, respectively, which subsequently led to the significant improvement of the DC conductivity of such PPy nanostructures. The highest conductivity of 175 S cm^{-1} was obtained for 1-D PPy synthesized at frozen condition (at −24 °C). This is the highest DC conductivity obtained for the powder PPy reported in the literature till now. The temperature dependence of conductivity of 1-D PPy pointed out that the 3-D variable range hopping is the charge transport mechanism in such fibrillar structure. This form of PPy possess an extended delocalization of carriers and allows for a high level of doping in the molecularly well-ordered domains. AC conductivity was found to be frequency independent that suggests the charge transport proceeds via homogeneous and compact grains.
- Thin PANI/PVP films prepared by spiral bar coating of corresponding colloidal particles reached the conductivity values of 7×10^{-5} S cm^{-1} and 5×10^{-3} S cm^{-1} when doped with PA and HCl, respectively. The conductivity of these films was found to decrease with increasing concentration of PVP due to the increased content of the non-conducting fraction. Additionally, it was found that the films with higher conductivity showed higher electrochemical activity.
- The broad band impedance spectroscopy recorded on the series of PPDA/MMT composites with different monomer-to-MMT ratio showed that

two different types of mechanisms are involved in the charge transport. In the low temperature range (173 - 273 K) there is correlated barrier hopping of polarons while ion transport is dominant in the higher temperature range (273-433 K).

- Electrochemical characterization of four Fe-MSPs containing various linkers showed that Fe-Tt has the best coloration efficiency (641 $cm^2\ C^{-1}$). This MSPs showed also the quasi-reversible redox process accompanied with disappearance of the MLCT band due to the oxidation of Fe^{2+} to Fe^{3+}. An ECD was successfully fabricated that showed the optical contrast around 60% at 637 nm and a good stability up to 100 repeating cycles.

Bibliography

1. Gueye, M.N.; Carella, A.; Faure-Vincent, J.; Demadrille, R.; Simonato, J.-P. Progress in Understanding Structure and Transport Properties of PEDOT-Based Materials: A Critical Review. *Progress in Materials Science* **2020**, *108*, 100616, doi:https://doi.org/10.1016/j.pmatsci.2019.100616.
2. Bredas, J.L.; Silbey, R.; Boudreaux, D.S.; Chance, R.R. Chain-Length Dependence of Electronic and Electrochemical Properties of Conjugated Systems: Polyacetylene, Polyphenylene, Polythiophene, and Polypyrrole | *Journal of the American Chemical Society* DOI: 10.1021/ja00360a004.
3. MacDiarmid, A.G. "Synthetic Metals": A Novel Role for Organic Polymers (Nobel Lecture). *Angewandte Chemie International Edition* **2001**, *40*, 2581–2590, doi:10.1002/1521-3773(20010716)40:14<2581::AID-ANIE2581>3.0.CO;2-2.
4. Ćirić-Marjanović, G. Recent Advances in Polyaniline Research: Polymerization Mechanisms, Structural Aspects, Properties and Applications. *Synthetic Metals* **2013**, *177*, 1–47, doi:10.1016/j.synthmet.2013.06.004.
5. Wang, L.-X.; Li, X.-G.; Yang, Y.-L. Preparation, Properties and Applications of Polypyrroles. *Reactive and Functional Polymers* **2001**, *47*, 125–139, doi:10.1016/S1381-5148(00)00079-1.
6. Kirchmeyer, S.; Reuter, K. Scientific Importance, Properties and Growing Applications of Poly(3,4-Ethylenedioxythiophene). *J. Mater. Chem.* **2005**, *15*, 2077–2088, doi:10.1039/B417803N.
7. Cataldo, F. On the Polymerization of P-Phenylenediamine. *European Polymer Journal* **1996**, *32*, 43–50, doi:10.1016/0014-3057(95)00118-2.
8. Minisy, I.M.; Gavrilov, N.; Acharya, U.; Morávková, Z.; Unterweger, C.; Mičušík, M.; Filippov, S.K.; Kredatusová, J.; Pašti, I.A.; Breitenbach, S.; et al. Tailoring of Carbonized Polypyrrole Nanotubes Core by Different Polypyrrole Shells for Oxygen Reduction Reaction Selectivity Modification. *Journal of Colloid and Interface Science* **2019**, *551*, 184–194, doi:10.1016/j.jcis.2019.04.064.
9. Acharya, U.; Bober, P.; Trchová, M.; Zhigunov, A.; Stejskal, J.; Pfleger, J. Synergistic Conductivity Increase in Polypyrrole/Molybdenum Disulfide Composite. *Polymer* **2018**, *150*, 130–137, doi:10.1016/j.polymer.2018.07.004.
10. Li, Y.; Bober, P.; Apaydin, D.H.; Syrový, T.; Sariciftci, N.S.; Hromádková, J.; Sapurina, I.; Trchová, M.; Stejskal, J. Colloids of Polypyrrole Nanotubes/Nanorods: A Promising Conducting Ink. *Synthetic Metals* **2016**, *221*, 67–74, doi:10.1016/j.synthmet.2016.10.007.
11. Kašpárková, V.; Jasenská, D.; Capáková, Z.; Maráková, N.; Stejskal, J.; Bober, P.; Lehocký, M.; Humpolíček, P. Polyaniline Colloids Stabilized with Bioactive Polysaccharides: Non-Cytotoxic Antibacterial Materials. *Carbohydrate Polymers* **2019**, *219*, 423–430, doi:10.1016/j.carbpol.2019.05.038.
12. Li, C.; Bai, H.; Shi, G. Conducting Polymer Nanomaterials: Electrosynthesis and Applications. *Chem. Soc. Rev.* **2009**, *38*, 2397–2409, doi:10.1039/B816681C.
13. Hutchison, G.R.; Zhao, Y.-J.; Delley, B.; Freeman, A.J.; Ratner, M.A.; Marks, T.J. Electronic Structure of Conducting Polymers: Limitations of Oligomer Extrapolation Approximations and Effects of Heteroatoms. *Phys. Rev. B* **2003**, *68*, 035204, doi:10.1103/PhysRevB.68.035204.
14. Heeger, A.J. Charge Storage in Conducting Polymers: Solitons, Polarons, and Bipolarons. *Polym J* **1985**, *17*, 201–208, doi:10.1295/polymj.17.201.

15. Heeger, A.J.; Kivelson, S.; Schrieffer, J.R.; Su, W.-P. Solitons in Conducting Polymers. *Rev. Mod. Phys.* **1988**, *60*, 781–850, doi:10.1103/RevModPhys.60.781.
16. Bredas, J.L.; Street, G.B. Polarons, Bipolarons, and Solitons in Conducting Polymers. *Acc. Chem. Res.* **1985**, *18*, 309–315, doi:10.1021/ar00118a005.
17. Zhao, Y.; Yang, Q.; Cheng, Q.; Ai, J.; Feng, M.; Wang, C.; Lv, X.; He, M.; Chen, Y. Construction of Conductive Hydroxyethyl Cellulose/Soy Protein Isolate/Polypyrrole Composite Sponges and Their Performances. *Cellulose* **2021**, *28*, 8527–8539, doi:10.1007/s10570-021-04074-4.
18. Milakin, K.A.; Capáková, Z.; Acharya, U.; Vajďák, J.; Morávková, Z.; Hodan, J.; Humpolíček, P.; Bober, P. Biocompatible and Antibacterial Gelatin-Based Polypyrrole Cryogels. *Polymer* **2020**, *197*, 122491, doi:10.1016/j.polymer.2020.122491.
19. Bober, P.; Stejskal, J.; Špírková, M.; Trchová, M.; Varga, M.; Prokeš, J. Conducting Polyaniline–Montmorillonite Composites. *Synthetic Metals* **2010**, *160*, 2596–2604, doi:10.1016/j.synthmet.2010.10.010.
20. Kazim, S.; Ahmad, S.; Pfleger, J.; Plestil, J.; Joshi, Y.M. Polyaniline–Sodium Montmorillonite Clay Nanocomposites: Effect of Clay Concentration on Thermal, Structural, and Electrical Properties. *J Mater Sci* **2012**, *47*, 420–428, doi:10.1007/s10853-011-5815-y.
21. Sajedi-Moghaddam, A.; Saievar-Iranizad, E.; Pumera, M. Two-Dimensional Transition Metal Dichalcogenide/Conducting Polymer Composites: Synthesis and Applications. *Nanoscale* **2017**, *9*, 8052–8065, doi:10.1039/C7NR02022H.
22. Shaikh, N.S.; Ubale, S.B.; Mane, V.J.; Shaikh, Jasmin.S.; Lokhande, Vaibhav.C.; Praserthdam, S.; Lokhande, C.D.; Kanjanaboos, P. Novel Electrodes for Supercapacitor: Conducting Polymers, Metal Oxides, Chalcogenides, Carbides, Nitrides, MXenes, and Their Composites with Graphene. *Journal of Alloys and Compounds* **2022**, *893*, 161998, doi:10.1016/j.jallcom.2021.161998.
23. Gangopadhyay, R.; De, A. Conducting Polymer Nanocomposites: A Brief Overview. *Chem. Mater.* **2000**, *12*, 608–622, doi:10.1021/cm990537f.
24. Anantha-Iyengar, G.; Shanmugasundaram, K.; Nallal, M.; Lee, K.-P.; Whitcombe, M.J.; Lakshmi, D.; Sai-Anand, G. Functionalized Conjugated Polymers for Sensing and Molecular Imprinting Applications. *Progress in Polymer Science* **2019**, *88*, 1–129, doi:10.1016/j.progpolymsci.2018.08.001.
25. Syrový, T.; Kuberský, P.; Sapurina, I.; Pretl, S.; Bober, P.; Syrová, L.; Hamáček, A.; Stejskal, J. Gravure-Printed Ammonia Sensor Based on Organic Polyaniline Colloids. *Sensors and Actuators B: Chemical* **2016**, *225*, 510–516, doi:10.1016/j.snb.2015.11.062.
26. Cheng, M.; Xia, J.; Hu, J.; Liu, Q.; Wei, T.; Ling, Y.; Li, W.; Liu, B. Nitrogen and Oxygen Codoped Carbon Anode Fabricated Facilely from Polyaniline Coated Cellulose Nanocrystals for High-Performance Li-Ion Batteries. *ACS Appl. Energy Mater.* **2021**, *4*, 9902–9912, doi:10.1021/acsaem.1c01900.
27. Naskar, P.; Maiti, A.; Chakraborty, P.; Kundu, D.; Biswas, B.; Banerjee, A. Chemical Supercapacitors: A Review Focusing on Metallic Compounds and Conducting Polymers. *J. Mater. Chem. A* **2021**, *9*, 1970–2017, doi:10.1039/D0TA09655E.
28. Wang, Z.; Zhu, M.; Pei, Z.; Xue, Q.; Li, H.; Huang, Y.; Zhi, C. Polymers for Supercapacitors: Boosting the Development of the Flexible and Wearable Energy Storage. *Materials Science and Engineering: R: Reports* **2020**, *139*, 100520, doi:10.1016/j.mser.2019.100520.
29. Meng, Q.; Cai, K.; Chen, Y.; Chen, L. Research Progress on Conducting Polymer Based Supercapacitor Electrode Materials. *Nano Energy* **2017**, *36*, 268–285, doi:10.1016/j.nanoen.2017.04.040.

30. Helgesen, M.; Søndergaard, R.; Krebs, F.C. Advanced Materials and Processes for Polymer Solar Cell Devices. *J. Mater. Chem.* **2009**, *20*, 36–60, doi:10.1039/B913168J.
31. Wu, K.; Gui, T.; Dong, J.; Luo, J.; Liu, R. Synthesis of Robust Polyaniline Microcapsules via UV-Initiated Emulsion Polymerization for Self-Healing and Anti-Corrosion Coating. *Progress in Organic Coatings* **2022**, *162*, 106592, doi:10.1016/j.porgcoat.2021.106592.
32. Yuan, X.-T.; Wu, L.; Geng, H.-Z.; Wang, L.; Wang, W.; Yuan, X.-S.; He, B.; Jiang, Y.-X.; Ning, Y.; Zhu, Z.-R.; et al. Polyaniline/Polysulfone Ultrafiltration Membranes with Improved Permeability and Anti-Fouling Behavior. *Journal of Water Process Engineering* **2021**, *40*, 101903, doi:10.1016/j.jwpe.2020.101903.
33. Bobacka, J. Conducting Polymer-Based Solid-State Ion-Selective Electrodes. *Electroanalysis* **2006**, *18*, 7–18, doi:10.1002/elan.200503384.
34. Hu, F.; Yan, B.; Sun, G.; Xu, J.; Gu, Y.; Lin, S.; Zhang, S.; Liu, B.; Chen, S. Conductive Polymer Nanotubes for Electrochromic Applications. *ACS Appl. Nano Mater.* **2019**, *2*, 3154–3160, doi:10.1021/acsanm.9b00472.
35. Bayat, M.; Izadan, H.; Santiago, S.; Estrany, F.; Dinari, M.; Semnani, D.; Alemán, C.; Guirado, G. Study on the Electrochromic Properties of Polypyrrole Layers Doped with Different Dye Molecules. *Journal of Electroanalytical Chemistry* **2021**, *886*, 115113, doi:10.1016/j.jelechem.2021.115113.
36. Li, S.; Zeng, F.; Chen, C.; Liu, H.; Tang, G.; Gao, S.; Song, C.; Lin, Y.; Pan, F.; Guo, D. Synaptic Plasticity and Learning Behaviours Mimicked through Ag Interface Movement in an Ag/Conducting Polymer/Ta Memristive System. *J. Mater. Chem. C* **2013**, *1*, 5292–5298, doi:10.1039/C3TC30575A.
37. Prudnikov, N.V.; Lapkin, D.A.; Emelyanov, A.V.; Minnekhanov, A.A.; Malakhova, Y.N.; Chvalun, S.N.; Demin, V.A.; Erokhin, V.V. Associative STDP-like Learning of Neuromorphic Circuits Based on Polyaniline Memristive Microdevices. *J. Phys. D: Appl. Phys.* **2020**, *53*, 414001, doi:10.1088/1361-6463/ab9262.
38. Lin, P.; Yan, F. Organic Thin-Film Transistors for Chemical and Biological Sensing. *Advanced Materials* **2012**, *24*, 34–51, doi:10.1002/adma.201103334.
39. Distler, T.; Boccaccini, A.R. 3D Printing of Electrically Conductive Hydrogels for Tissue Engineering and Biosensors – A Review. *Acta Biomaterialia* **2020**, *101*, 1–13, doi:10.1016/j.actbio.2019.08.044.
40. Balint, R.; Cassidy, N.J.; Cartmell, S.H. Conductive Polymers: Towards a Smart Biomaterial for Tissue Engineering. *Acta Biomaterialia* **2014**, *10*, 2341–2353, doi:10.1016/j.actbio.2014.02.015.
41. Atkins, P.W.; Friedman, R.S. Molecular Quantum Mechanics - Oxford University Press.
42. Le, T.-H.; Yoon, H. Fundamentals of Conjugated Polymer Nanostructures. In *Conjugated Polymer Nanostructures for Energy Conversion and Storage Applications*; John Wiley & Sons, Ltd, 2021; pp. 1–42 ISBN 978-3-527-82011-5.
43. Anderson, P.W. Absence of Diffusion in Certain Random Lattices. *Phys. Rev.* **1958**, *109*, 1492–1505, doi:10.1103/PhysRev.109.1492.
44. Baranovski, S., Ed. *Charge Transport in Disordered Solids with Applications in Electronics*; 1st ed.; Wiley, 2006; ISBN 978-0-470-09504-1.
45. Kivelson, S.; Heeger, A.J. Intrinsic Conductivity of Conducting Polymers. *Synthetic Metals* **1988**, *22*, 371–384, doi:10.1016/0379-6779(88)90108-7.
46. Mott, N.F.; Davis, E.A.; Mott, N.F.; Davis, E.A. *Electronic Processes in Non-Crystalline Materials*; Oxford Classic Texts in the Physical Sciences; Oxford University Press: Oxford, New York, 2012; ISBN 978-0-19-964533-6.
47. Shklovskii, B.I.; Efros, A.L. *Electronic Properties of Doped Semiconductors*; Springer Series

in Solid-State Sciences; Springer: Berlin, Heidelberg, 1984; Vol. 45; ISBN 978-3-662-02405-8.
48. Epstein, A.J.; Joo, J.; Kohlman, R.S.; Du, G.; MacDiarmid, A.G.; Oh, E.J.; Min, Y.; Tsukamoto, J.; Kaneko, H.; Pouget, J.P. Inhomogeneous Disorder and the Modified Drude Metallic State of Conducting Polymers. *Synthetic Metals* **1994**, *65*, 149–157, doi:10.1016/0379-6779(94)90176-7.
49. Sheng, P.; Klafter, J. Hopping Conductivity in Granular Disordered Systems. *Phys. Rev. B* **1983**, *27*, 2583–2586, doi:10.1103/PhysRevB.27.2583.
50. Sheng, P. Fluctuation-Induced Tunneling Conduction in Disordered Materials. *Phys. Rev. B* **1980**, *21*, 2180–2195, doi:10.1103/PhysRevB.21.2180.
51. Kaiser, A.B.; Düsberg, G.; Roth, S. Heterogeneous Model for Conduction in Carbon Nanotubes. *Phys. Rev. B* **1998**, *57*, 1418–1421, doi:10.1103/PhysRevB.57.1418.
52. Mizes, H.A.; Conwell, E. M. Stability of Polarons in Conducting Polymers 10.1103/Physrevlett.70.1505 · OA.Mg.
53. Baughman, R.H.; Shacklette, L.W. Conductivity as a Function of Conjugation Length: Theory and Experiment for Conducting Polymer Complexes. *Phys. Rev. B* **1989**, *39*, 5872–5886, doi:10.1103/PhysRevB.39.5872.
54. Electronic Properties of Polymers and Related Compounds: Proceedings of an International Winter School, Kirchberg, Tirol, February 23 – March 1, 1985 | S. Roth (Auth.), Professor Dr. Hans Kuzmany, Professor Dr. Michael Mehring, Dr. Siegmar Roth (Eds.) |.
55. Sinkkonen, J. DC Conductivity of a Random Barrier Network. *physica status solidi (b)* **1980**, *102*, 621–627, doi:10.1002/pssb.2221020222.
56. Paasch, G.; Karg, S.; Schimmel, Th.; Riess, W.; Schwoerer, M. Comparison of Heterogeneous Polymer Models for the Explanation of Charge Transport in Naarmann-Polyacetylene. *Synthetic Metals* **1993**, *57*, 4872–4877, doi:10.1016/0379-6779(93)90831-G.
57. Zabrodskii, A.G.; Zinov'eva, K.N. Low-Temperatureconductivity and Metal-Insulator Transition in Compensate n-Ge. **1984**.
58. Ahlskog, M.; Reghu, M.; Heeger, A.J. The Temperature Dependence of the Conductivity in the Critical Regime of the Metal - Insulator Transition in Conducting Polymers. *Journal of Physics Condensed Matter*, *9*, 4145–4156, doi:10.1088/0953-8984/9/20/014.
59. McMillan, W.L. Scaling Theory of the Metal-Insulator Transition in Amorphous Materials. *Phys. Rev. B* **1981**, *24*, 2739–2743, doi:10.1103/PhysRevB.24.2739.
60. Larkin, A.I.; Khmel'nitskii, D.E. Activation Conductivity in Disordered Systems with Large Localization Length. **1982**.
61. Miller, A.; Abrahams, E. Impurity Conduction at Low Concentrations. *Phys. Rev.* **1960**, *120*, 745–755, doi:10.1103/PhysRev.120.745.
62. Marcus, R.A. Electron Transfer Reactions in Chemistry. Theory and Experiment. *Rev. Mod. Phys.* **1993**, *65*, 599–610, doi:10.1103/RevModPhys.65.599.
63. Noriega, R.; Salleo, A. Charge Transport Theories in Organic Semiconductors. In *Organic Electronics II*; John Wiley & Sons, Ltd, 2012; pp. 67–104 ISBN 978-3-527-64021-8.
64. Coropceanu, V.; Cornil, J.; da Silva Filho, D.A.; Olivier, Y.; Silbey, R.; Brédas, J.-L. Charge Transport in Organic Semiconductors. *Chem. Rev.* **2007**, *107*, 926–952, doi:10.1021/cr050140x.
65. Acharya, U.; Bober, P.; Thottappali, M.A.; Morávková, Z.; Konefał, M.; Pfleger, J. Synthesis and Impedance Spectroscopy of Poly(p-Phenylenediamine)/Montmorillonite Composites. *Polymers* **2021**, *13*, 3132, doi:10.3390/polym13183132.
66. Dyre, J.C. The Random Free-energy Barrier Model for Ac Conduction in Disordered Solids. *Journal of Applied Physics* **1988**, *64*, 2456–2468, doi:10.1063/1.341681.

67. Montroll, E.W.; Weiss, G.H. Random Walks on Lattices. II. *Journal of Mathematical Physics* **2004**, *6*, 167–181, doi:10.1063/1.1704269.
68. Moynihan, C.T. Analysis of Electrical Relaxation in Glasses and Melts with Large Concentrations of Mobile Ions. *Journal of Non-Crystalline Solids* **1994**, *172–174*, 1395–1407, doi:10.1016/0022-3093(94)90668-8.
69. Jonscher, A.K. The 'Universal' Dielectric Response. *Nature* **1977**, *267*, 673–679, doi:10.1038/267673a0.
70. Ramachandran, L.; Lonjon, A.; Demont, P.; Dantras, E.; Lacabanne, C. Conduction Mechanisms in P(VDF-TrFE)/Gold Nanowire Composites: Tunnelling and Thermally-Activated Hopping Process near the Percolation Threshold. *Mater. Res. Express* **2016**, *3*, 085027, doi:10.1088/2053-1591/3/8/085027.
71. Ben Taher, Y.; Oueslati, A.; Maaloul, N.K.; Khirouni, K.; Gargouri, M. Conductivity Study and Correlated Barrier Hopping (CBH) Conduction Mechanism in Diphosphate Compound. *Appl. Phys. A* **2015**, *120*, 1537–1543, doi:10.1007/s00339-015-9353-3.
72. Mahmoud, K.H.; Abdel-Rahim, F.M.; Atef, K.; Saddeek, Y.B. Dielectric Dispersion in Lithium–Bismuth-Borate Glasses. *Current Applied Physics* **2011**, *11*, 55–60, doi:10.1016/j.cap.2010.06.018.
73. Lehn, J.-M. Supramolecular Chemistry—Scope and Perspectives Molecules, Supermolecules, and Molecular Devices(Nobel Lecture). *Angew. Chem. Int. Ed. Engl.* **1988**, *27*, 89–112, doi:10.1002/anie.198800891.
74. Higuchi, M. *Metallo-Supramolecular Polymers: Synthesis, Properties, and Device Applications*; NIMS Monographs; Springer Japan: Tokyo, 2019; ISBN 978-4-431-56889-6.
75. Ninomiya, Y.; Yoshida, T.; Higuchi, M. Electrochromic Fe(II)-Based Metallo-Supramolecular Polymers: Color Modulation by Spacer Modification in Bisterpyridine Ligand. *Chem. Lett.* **2020**, *49*, 1003–1005, doi:10.1246/cl.200307.
76. Santra, D.C.; Mondal, S.; Yoshida, T.; Ninomiya, Y.; Higuchi, M. Ru(II)-Based Metallo-Supramolecular Polymer with Tetrakis(N-Methylbenzimidazolyl)Bipyridine for a Durable, Nonvolatile, and Electrochromic Device Driven at 0.6 V. *ACS Appl. Mater. Interfaces* **2021**, *13*, 31153–31162, doi:10.1021/acsami.1c07275.
77. Tu, T.-H.; Chan, Y.-T. Synthesis of Terpyridine End-Modified Polystyrenes through ATRP for Facile Construction of Metallo-Supramolecular P3HT-b-PS Diblock Copolymers. *Polymers* **2020**, *12*, 2842, doi:10.3390/polym12122842.
78. Duerrbeck, A.; Gorelik, S.; Hobley, J.; Yong, A.M.; Subramanian, G.S.; Hor, A.; Long, N. New Solid-State Eu(III)-Containing Metallo-Supramolecular Polymers: Morphology Control and Optical Wave-Guiding Properties. *J. Mater. Chem. C* **2015**, *3*, 8992–9002, doi:10.1039/C5TC01703C.
79. A Green Copper-Based Metallo-Supramolecular Polymer: Synthesis, Structure, and Electrochromic Properties - Hossain - 2013 - Chemistry – An Asian Journal - Wiley Online Library.
80. Bera, M.K.; Chakraborty, C.; Rana, U.; Higuchi, M. Electrochromic Os(II)-Based Metallo-Supramolecular Polymers. *Macromolecular Rapid Communications* **2018**, *39*, 1800415, doi:10.1002/marc.201800415.
81. Chernyshev, A.; Acharya, U.; Pfleger, J.; Trhlíková, O.; Zedník, J.; Vohlídal, J. Iron (II) Metallo-Supramolecular Polymers Based on Thieno[3,2-b]Thiophene for Electrochromic Applications. *Polymers* **2021**, *13*, 362, doi:10.3390/polym13030362.
82. Deb, S.K. Optical and Photoelectric Properties and Colour Centres in Thin Films of Tungsten Oxide. *The Philosophical Magazine: A Journal of Theoretical Experimental and Applied Physics* **1973**, *27*, 801–822, doi:10.1080/14786437308227562.
83. Abidin, T.; Zhang, Q.; Wang, K.-L.; Liaw, D.-J. Recent Advances in Electrochromic

Polymers. *Polymer* **2014**, *55*, 5293–5304, doi:10.1016/j.polymer.2014.08.046.
84. Handbook of Inorganic Electrochromic Materials - 1st Edition Editor: C.G. Granqvist. Available online: https://www.elsevier.com/books/handbook-of-inorganic-electrochromic-materials/granqvist/978-0-444-89930-9 .
85. Agrawal, A.; Susut, C.; Stafford, G.; Bertocci, U.; McMorran, B.; Lezec, H.J.; Talin, A.A. An Integrated Electrochromic Nanoplasmonic Optical Switch. *Nano Lett.* **2011**, *11*, 2774–2778, doi:10.1021/nl201064x.
86. Madasamy, K.; Velayutham, D.; Suryanarayanan, V.; Kathiresan, M.; Ho, K.-C. Viologen-Based Electrochromic Materials and Devices. *J. Mater. Chem. C* **2019**, *7*, 4622–4637, doi:10.1039/C9TC00416E.
87. Neo, W.T.; Ye, Q.; Chua, S.-J.; Xu, J. Conjugated Polymer-Based Electrochromics: Materials, Device Fabrication and Application Prospects. *J. Mater. Chem. C* **2016**, *4*, 7364–7376, doi:10.1039/C6TC01150K.
88. Kim, J.; Rémond, M.; Kim, D.; Jang, H.; Kim, E. Electrochromic Conjugated Polymers for Multifunctional Smart Windows with Integrative Functionalities. *Advanced Materials Technologies* **2020**, *5*, 1900890, doi:10.1002/admt.201900890.
89. Nie, G.; Zhou, L.; Guo, Q.; Zhang, S. A New Electrochromic Material from an Indole Derivative and Its Application in High-Quality Electrochromic Devices. *Electrochemistry Communications* **2010**, *12*, 160–163, doi:10.1016/j.elecom.2009.11.013.
90. Winter, A.; Schubert, U.S. Synthesis and Characterization of Metallo-Supramolecular Polymers. *Chem. Soc. Rev.* **2016**, *45*, 5311–5357, doi:10.1039/C6CS00182C.
91. Wade, C.R.; Li, M.; Dincă, M. Facile Deposition of Multicolored Electrochromic Metal–Organic Framework Thin Films. *Angewandte Chemie International Edition* **2013**, *52*, 13377–13381, doi:10.1002/anie.201306162.
92. Mjejri, I.; Doherty, C.M.; Rubio-Martinez, M.; Drisko, G.L.; Rougier, A. Double-Sided Electrochromic Device Based on Metal–Organic Frameworks. *ACS Appl. Mater. Interfaces* **2017**, *9*, 39930–39934, doi:10.1021/acsami.7b13647.
93. Sarkar, M.; Dutta, T.K.; Patra, A. Two-Dimensional Covalent Organic Frameworks for Electrochromic Switching. *Chemistry – An Asian Journal* **2021**, *16*, 3055–3067, doi:10.1002/asia.202100815.
94. Salles, P.; Pinto, D.; Hantanasirisakul, K.; Maleski, K.; Shuck, C.E.; Gogotsi, Y. Electrochromic Effect in Titanium Carbide MXene Thin Films Produced by Dip-Coating. *Advanced Functional Materials* **2019**, *29*, 1809223, doi:10.1002/adfm.201809223.
95. Lee, S.J.; Choi, D.S.; Kang, S.H.; Yang, W.S.; Nahm, S.; Han, S.H.; Kim, T. VO2/WO3-Based Hybrid Smart Windows with Thermochromic and Electrochromic Properties. *ACS Sustainable Chem. Eng.* **2019**, *7*, 7111–7117, doi:10.1021/acssuschemeng.9b00052.
96. Wang, F.-X.; Wang, M.-J.; Liu, H.-C.; Zhang, Y.-L.; Lin, Q.-H.; Chen, T.; Sun, L.-N. Multifunctional Self-Powered E-Skin with Tactile Sensing and Visual Warning for Detecting Robot Safety. *Advanced Materials Interfaces* **2020**, *7*, 2000536, doi:10.1002/admi.202000536.
97. A Review of Organic Electrochromic Fabric Devices - Kline - 2014 - Coloration Technology - Wiley Online Library Available online: https://onlinelibrary.wiley.com/doi/full/10.1111/cote.12079.
98. Richardson, T.J. New Electrochromic Mirror Systems. *Solid State Ionics* **2003**, *165*, 305–308, doi:10.1016/j.ssi.2003.08.047.
99. Zhao, J.; Tian, Y.; Wang, Z.; Cong, S.; Zhou, D.; Zhang, Q.; Yang, M.; Zhang, W.; Geng, F.; Zhao, Z. Trace H2O2-Assisted High-Capacity Tungsten Oxide Electrochromic Batteries with Ultrafast Charging in Seconds. *Angewandte Chemie International Edition* **2016**, *55*, 7161–7165, doi:10.1002/anie.201602657.

100. Wei, D.; Scherer, M.R.J.; Bower, C.; Andrew, P.; Ryhänen, T.; Steiner, U. A Nanostructured Electrochromic Supercapacitor. *Nano Lett.* **2012**, *12*, 1857–1862, doi:10.1021/nl2042112.
101. Tian, Y.; Cong, S.; Su, W.; Chen, H.; Li, Q.; Geng, F.; Zhao, Z. Synergy of W18O49 and Polyaniline for Smart Supercapacitor Electrode Integrated with Energy Level Indicating Functionality. *Nano Lett.* **2014**, *14*, 2150–2156, doi:10.1021/nl5004448.
102. Yeh, M.-H.; Lin, L.; Yang, P.-K.; Wang, Z.L. Motion-Driven Electrochromic Reactions for Self-Powered Smart Window System. *ACS Nano* **2015**, *9*, 4757–4765, doi:10.1021/acsnano.5b00706.
103. Song, R.; Li, G.; Zhang, Y.; Rao, B.; Xiong, S.; He, G. Novel Electrochromic Materials Based on Chalcogenoviologens for Smart Windows, E-Price Tag and Flexible Display with Improved Reversibility and Stability. *Chemical Engineering Journal* **2021**, *422*, 130057, doi:10.1016/j.cej.2021.130057.
104. Yang, B.; Ma, D.; Zheng, E.; Wang, J. A Self-Rechargeable Electrochromic Battery Based on Electrodeposited Polypyrrole Film. *Solar Energy Materials and Solar Cells* **2019**, *192*, 1–7, doi:10.1016/j.solmat.2018.12.011.
105. Li, G.; Zhang, B.; Wang, J.; Zhao, H.; Ma, W.; Xu, L.; Zhang, W.; Zhou, K.; Du, Y.; He, G. Electrochromic Poly(Chalcogenoviologen)s as Anode Materials for High-Performance Organic Radical Lithium-Ion Batteries. *Angewandte Chemie International Edition* **2019**, *58*, 8468–8473, doi:10.1002/anie.201903152.
106. Singh, S.B.; Tran, D.T.; Jeong, K.-U.; Kim, N.H.; Lee, J.H. A Flexible and Transparent Zinc-Nanofiber Network Electrode for Wearable Electrochromic, Rechargeable Zn-Ion Battery. *Small* **2022**, *18*, 2104462, doi:10.1002/smll.202104462.
107. Yue, Z.; Wang, Y.; Lin, Y.; Jia, C. Fully Integrated Pressure-Controlled Electrochromic E-Skins. *J. Mater. Chem. A* **2021**, *9*, 9134–9144, doi:10.1039/D1TA00380A.
108. Howard, E.L.; Österholm, A.M.; Shen, D.E.; Panchumarti, L.P.; Pinheiro, C.; Reynolds, J.R. Cost-Effective, Flexible, and Colorful Dynamic Displays: Removing Underlying Conducting Layers from Polymer-Based Electrochromic Devices. *ACS Appl. Mater. Interfaces* **2021**, *13*, 16732–16743, doi:10.1021/acsami.1c00463.
109. Österholm, A.M.; Shen, D.E.; Kerszulis, J.A.; Bulloch, R.H.; Kuepfert, M.; Dyer, A.L.; Reynolds, J.R. Four Shades of Brown: Tuning of Electrochromic Polymer Blends Toward High-Contrast Eyewear. *ACS Appl. Mater. Interfaces* **2015**, *7*, 1413–1421, doi:10.1021/am507063d.
110. Kondo, Y.; Tanabe, H.; Kudo, H.; Nakano, K.; Otake, T. Electrochromic Type E-Paper Using Poly(1H-Thieno[3,4-d]Imidazol-2(3H)-One) Derivatives by a Novel Printing Fabrication Process. *Materials* **2011**, *4*, 2171–2182, doi:10.3390/ma4122171.
111. Wang, K.; Tao, K.; Jiang, R.; Zhang, H.; Liang, L.; Gao, J.; Cao, H. A Self-Bleaching Electrochromic Mirror Based on Metal Organic Frameworks. *Materials* **2021**, *14*, 2771, doi:10.3390/ma14112771.
112. Wang, H.; Barrett, M.; Duane, B.; Gu, J.; Zenhausern, F. Materials and Processing of Polymer-Based Electrochromic Devices. *Materials Science and Engineering: B* **2018**, *228*, 167–174, doi:10.1016/j.mseb.2017.11.016.
113. Hybrid Materials and Polymer Electrolytes for Electrochromic Device Applications - Thakur - 2012 - Advanced Materials - Wiley Online Library Available online: https://onlinelibrary.wiley.com/doi/full/10.1002/adma.201200213 .
114. Pettersson, H.; Gruszecki, T.; Johansson, L.-H.; Edwards, M.O.M.; Hagfeldt, A.; Matuszczyk, T. Direct-Driven Electrochromic Displays Based on Nanocrystalline Electrodes. *Displays* **2004**, *25*, 223–230, doi:10.1016/j.displa.2004.09.015.
115. Bechinger, C.; Bullock, J.N.; Zhang, J. -G.; Tracy, C.E.; Benson, D.K.; Deb, S.K.; Branz,

H.M. Low-voltage Electrochromic Device for Photovoltaic-powered Smart Windows. *Journal of Applied Physics* **1996**, *80*, 1226–1232, doi:10.1063/1.363731.
116. Banaszczyk, J.; Schwarz, A.; De Mey, G.; Van Langenhove, L. The Van der Pauw method for sheet resistance measurements of polypyrrole-coated para-aramide woven fabrics. *Journal of Applied Polymer Science* **2010**, *117*, 2553–2558, doi:10.1002/app.32186.
117. van der PAUW, L.J. A Method of Measuring Specific Resistivity and Hall Effect of Discs of Arbitrary Shape. In *Semiconductor Devices: Pioneering Papers*; WORLD SCIENTIFIC, 1991; pp. 174–182 ISBN 978-981-02-0209-5.
118. Resistivity. In *Semiconductor Material and Device Characterization*; John Wiley & Sons, Ltd, 2005; pp. 1–59 ISBN 978-0-471-74909-7.
119. Wang, J.; Wu, Z.; Hu, K.; Chen, X.; Yin, H. High Conductivity Graphene-like MoS2/Polyaniline Nanocomposites and Its Application in Supercapacitor. *Journal of Alloys and Compounds* **2015**, *619*, 38–43, doi:10.1016/j.jallcom.2014.09.008.
120. Stejskal, J.; Trchová, M.; Bober, P.; Morávková, Z.; Kopecký, D.; Vrňata, M.; Prokeš, J.; Varga, M.; Watzlová, E. Polypyrrole Salts and Bases: Superior Conductivity of Nanotubes and Their Stability towards the Loss of Conductivity by Deprotonation. *RSC Advances* **2016**, *6*, 88382–88391, doi:10.1039/C6RA19461C.
121. Li, Y.; Bober, P.; Trchová, M.; Stejskal, J. Polypyrrole Prepared in the Presence of Methyl Orange and Ethyl Orange: Nanotubes versus Globules in Conductivity Enhancement. *J. Mater. Chem. C* **2017**, *5*, 4236–4245, doi:10.1039/C7TC00206H.
122. Bober, P.; Stejskal, J.; Trchová, M.; Prokeš, J. The Preparation of Conducting Polyaniline–Silver and Poly(p-Phenylenediamine)–Silver Nanocomposites in Liquid and Frozen Reaction Mixtures. *J Solid State Electrochem* **2011**, *15*, 2361–2368, doi:10.1007/s10008-011-1414-8.
123. Peřinka, N.; Držková, M.; Randjelović, D.V.; Bondavalli, P.; Hajná, M.; Bober, P.; Syrový, T.; Bonnassieaux, Y.; Stejskal, J. Characterization of Polyaniline-Based Ammonia Gas Sensors Prepared by Means of Spray Coating and Ink-Jet Printing. *Sensor Letters* **2014**, *12*, 1620–1627, doi:10.1166/sl.2014.3362.
124. Bober, P.; Lindfors, T.; Pesonen, M.; Stejskal, J. Enhanced PH Stability of Conducting Polyaniline by Reprotonation with Perfluorooctanesulfonic Acid. *Synthetic Metals* **2013**, *178*, 52–55, doi:10.1016/j.synthmet.2013.07.002.
125. Elliott, S.R. A.c. Conduction in Amorphous Chalcogenide and Pnictide Semiconductors. *Advances in Physics* **1987**, *36*, 135–217, doi:10.1080/00018738700101971.
126. Liang, Y.; Strohecker, D.; Lynch, V.; Holliday, B.J.; Jones, R.A. A Thiophene-Containing Conductive Metallopolymer Using an Fe(II) Bis(Terpyridine) Core for Electrochromic Materials. *ACS Appl. Mater. Interfaces* **2016**, *8*, 34568–34580, doi:10.1021/acsami.6b11657.
127. Pai, S.; Schott, M.; Niklaus, L.; Posset, U.; G. Kurth, D. A Study of the Effect of Pyridine Linkers on the Viscosity and Electrochromic Properties of Metallo-Supramolecular Coordination Polymers. *Journal of Materials Chemistry C* **2018**, *6*, 3310–3321, doi:10.1039/C7TC04177B.
128. Kuai, Y.; Li, W.; Dong, Y.; Wong, W.-Y.; Yan, S.; Dai, Y.; Zhang, C. Multi-Color Electrochromism from Coordination Nanosheets Based on a Terpyridine-Fe(Ii) Complex. *Dalton Trans* **2019**, *48*, 15121–15126, doi:10.1039/c9dt02980j.
129. Mondal, S.; Ninomiya, Y.; Yoshida, T.; Mori, T.; Bera, M.K.; Ariga, K.; Higuchi, M. Dual-Branched Dense Hexagonal Fe(II)-Based Coordination Nanosheets with Red-to-Colorless Electrochromism and Durable Device Fabrication. *ACS Appl. Mater. Interfaces* **2020**, *12*, 31896–31903, doi:10.1021/acsami.0c05921.
130. Fabretto, M.; Vaithianathan, T.; Hall, C.; Murphy, P.; Innis, P.C.; Mazurkiewicz, J.; Wallace, G.G. Colouration Efficiency Measurements in Electrochromic Polymers: The

Importance of Charge Density. *Electrochemistry Communications* **2007**, *9*, 2032–2036, doi:10.1016/j.elecom.2007.05.035.

List of Figures

List of Tables

List of Abbreviations

AB	acid blue
AC	alternating current
ACN	acetonitrile
AFM	atomic force microscopy
BET	Brunauer-Emmett-Teller
CBH	correlated barrier hopping
CE	coloration efficiency
CELT	charge energy limited model
CP	conducting polymer
CTRW	continuous-time-random walk
DC	direct current
EC	electrochromism
ECD	electrochromic device
eV	electron volt
FIT	fluctuation-induced tunneling
FTIR	fourier-transform infra-red RAMAN
FTO	fluorine doped tin oxide
HCl	hydrochloric acid
HOMO	highest occupied molecular orbital
ITO	indium tin oxide
KWW	Kohlrausch-Williams-Watts
LMCT	ligand to metal charge transfer
LUMO	lowest unoccupied molecular orbital
MLCT	metal to ligand charge transfer
MMT	montmorillonite
MSP	metallo–supramolecular polymer
MTR	multiple trapping and releasing
NIR	near infra-red
OD	optical density
PA	polyacetylene
PANI	polyaniline
PEDOT	poly(3,4-ethylenedioxythiophene)
PPDA	poly(*p*-phenylenediamine)
PPy	polypyrrole
PVP	poly(*N*-vinylpyrrolidone)
RBN	random barrier network
SEM	scanning electron microscopy
TEM	transmission electron microscopy
TGA	thermogravimetric analysis
UV	ultra-violet
VRH	variable range hopping
XRD	X-ray diffraction

List of publications

1. **U. Acharya**, P. Bober, M. Trchová, A. Zhigunov, J. Stejskal, J. Pfleger, *Synergistic conductivity increase in polypyrrole/molybdenum disulfide composite*, Polymer 150 (**2018**) 130-137.
2. P. Bober, Y. Li, **U. Acharya**, Y. Panthi, J. Pfleger, P. Humpolíček, M. Trchová, J. Stejskal, *Acid Blue dyes in polypyrrole synthesis: the control of polymer morphology at nanoscale in the promotion of high conductivity and the reduction of cytotoxicity*, Synthetic Metals 237 (**2018**) 40-49.
3. I. M. Minisy, P. Bober, **U. Acharya**, M. Trchová, J. Hromádková, J. Pfleger, J. Stejskal,
   Cationic dyes as morphology-guiding agents for one-dimensional polypyrrole with improved conductivity, Polymer 174 (**2019**)11-17.
4. I. Minisy, **U. Acharya**, L. Kobera, M. Trchova, C. Unterweger, S. Breitenbach, J. Brus, J. Pfleger, J. Stejskal, P. Bober, *Highly conducting 1-D polypyrrole prepared in the presence of safranin,* Journal of Materials Chemistry C 35 (2020) 12140-12147.
5. A. Chernyshev†, **U. Acharya†,** J. Pfleger, O. Trhlíková, J. Zedník, J. Vohlídal, *Iron (II) metallo-supramolecular polymers based on thieno[3,2-b]thiophene for electrochromic applications,* Polymers 13 (2021) 362:1-16.
   † Both co-authors contributed equally to this work.
6. **U. Acharya**, P. Bober, M. A. Thottappali, Z. Morávková, M. Konefał, J. Pfleger, *Synthesis and impedance spectroscopy of poly(p-phenylenediamine)/montmorillonite composites,* Polymers 13 (2021) 3132:1-17.
7. K. A. Milakin, **U. Acharya**, I. M. Minisy, D. Tumacder, Z. Morávková, O. Taboubi, T. Syrový, L. Syrová, J. Pfleger, P. Bober, *Tuning of surface properties of conducting films casted from polyaniline-phytic acid-poly(N-vinylpyrrolidone) dispersions,* Progress in Organic Coatings 163 (2022) 106666:1-9.
8. B. Paruzel, J. Pfleger, J. Brus, M. Menšík, F. Piana, **U. Acharya**, *Impact of hydrogen bonds limited dipolar disorder in high-k polymer gate dielectric on charge carrier transport in OFET,* Polymers 12 (2020) 826:1-17.
9. P. Bober, N. Gavrilov, A. Kovalcik, M. Mičušík, C. Unterweger, I. A. Pašti, I. Šeděnková, **U. Acharya**, J. Pfleger, S. K. Filippov, J. Kuličeк, M. Omastová, S. Breitenbach, G. Ćirić-Marjanović, J. Stejskal, *Electrochemical properties of lignin/polypyrrole composites and their carbonized analogues,* Materials Chemistry and Physics 213 (2018) 352-361.

Attachments

A.1

U. Acharya, P. Bober, M. Trchová, A. Zhigunov, J. Stejskal, J. Pfleger, *Synergistic conductivity increase in polypyrrole/molybdenum disulfide composite*, Polymer 150 (**2018**) 130-137.

A.2

P. Bober, Y. Li, **U. Acharya**, Y. Panthi, J. Pfleger, P. Humpolíček, M. Trchová, J. Stejskal, *Acid Blue dyes in polypyrrole synthesis: the control of polymer morphology at nanoscale in the promotion of high conductivity and the reduction of cytotoxicity*, Synthetic Metals 237 (**2018**) 40-49.

A.3

I. M. Minisy, P. Bober, **U. Acharya**, M. Trchová, J. Hromádková, J. Pfleger, J. Stejskal, *Cationic dyes as morphology-guiding agents for one-dimensional polypyrrole with improved conductivity*, Polymer 174 (**2019**)11-17.

A.4

I. Minisy, **U. Acharya**, L. Kobera, M. Trchova, C. Unterweger, S. Breitenbach, J. Brus, J. Pfleger, J. Stejskal, P. Bober, *Highly conducting 1-D polypyrrole prepared in the presence of safranin*, Journal of Materials Chemistry C 35 (2020) 12140-12147.

A.5

A. Chernyshev†, **U. Acharya†,** J. Pfleger, O. Trhlíková, J. Zedník, J. Vohlídal, *Iron (II) metallo-supramolecular polymers based on thieno[3,2-b]thiophene for electrochromic applications*, Polymers 13 (2021) 362:1-16.
† Both co-authors contributed equally to this work.

A.6

U. Acharya, P. Bober, M. A. Thottappali, Z. Morávková, M. Konefał, J. Pfleger, *Synthesis and impedance spectroscopy of poly(p-phenylenediamine)/montmorillonite composites*, Polymers 13 (2021) 3132:1-17.

A.7

K. A. Milakin, **U. Acharya**, I. M. Minisy, D. Tumacder, Z. Morávková, O. Taboubi, T. Syrový, L. Syrová, J. Pfleger, P. Bober, *Tuning of surface properties of conducting films casted from polyaniline-phytic acid-poly(N-vinylpyrrolidone) dispersions*, Progress in Organic Coatings 163 (2022) 106666:1-9.